MECHANICAL EVALUATION OF ELECTRONIC PROPERTIES OF MATERIALS

A Thesis

by

NICHOLAS JOSEPH NUDO

Submitted to the Office of Graduate Studies of
Texas A&M University
in partial fulfillment of the requirements for the degree of

MASTER OF SCIENCE

May 2011

Major Subject: Mechanical Engineering

MECHANICAL EVALUATION OF ELECTRONIC PROPERTIES OF MATERIALS

A Thesis

by

NICHOLAS JOSEPH NUDO

Submitted to the Office of Graduate Studies of
Texas A&M University
in partial fulfillment of the requirements for the degree of

MASTER OF SCIENCE

Approved by:

Chair of Committee,	Hong Liang
Committee Members,	Miladin Radovic
	Philip Hemmer
Head of Department,	Dennis O'Neal

May 2011

Major Subject: Mechanical Engineering

ABSTRACT

Mechanical Evaluation of Electronic Properties of Materials. (May 2011)

Nicholas Joseph Nudo, B.S., Texas A&M University

Chair of Advisory Committee: Dr. Hong Liang

The present research focuses on the coupling of mechanical and electrical properties of materials and culminates in a direct connection between applied strain to thin-films, thin-film electron binding energy, the energy loss via plastic deformation provided by an indentation, and the substrate resistance. The methods used in this research include X-ray photoelectron spectroscopy (XPS), nanoindentation, digital optical microscopy, and sputter coat deposition.

It is discovered that there is a shift in electron binding energy on the scale of 0.2 eV to 1.4 eV in gold and palladium thin-films sputtered on polyvinylidene fluoride (PVDF) through the application of strain induced by a convex shape. There is a change in the area beneath the load-displacement curve measured via indentation from 5.55×10^{-10} J to 4.78×10^{-10} J when the gold-palladium thin-film sputtered on PVDF is changed from the flat arrangement to the convex arrangement. Furthermore, the strain also changed the electrical resistance of aluminum foil, which indicates that the substrate electrical resistance is affected by the induced strain. The internal resistance of a circuit developed for this research changed from 7.76 Ω for flat samples to 8.03 Ω and 8.33 Ω, for flat and convex samples, respectively. It is expected that the research can be used to estimate the strain in nanogears and other devices at small length scales.

DEDICATION

This thesis is dedicated to my parents, James & Laurel Nudo. Words cannot describe the love I have for them, nor the countless sacrifices they have made to ensure the wellbeing of me and my brother and sister.

ACKNOWLEDGEMENTS

I am tremendously grateful for the opportunities that Dr. Miladin Radovic and Dr. Hong Liang have given me as both an undergraduate student and a graduate student in the Department of Mechanical Engineering at Texas A&M University. As an undergraduate student in mechanical engineering, I enrolled in Dr. Radovic’s MEEN 222 Materials Science course in the Fall 2006 semester. I thoroughly enjoyed the course and desired to learn more about materials science and engineering. He sponsored me in the Undergraduate Summer Research Grants (USRG) program in the Summer 2007 semester, and has served as a mentor in the Material Advantage organization. Dr. Liang gave me the opportunity to participate in the National Consortium for MASINT Research Scholars Program for two consecutive years, 2007-2009, and served as a mentor through critical discussions regarding the nature of this thesis. I would also like to thank Dr. Philip Hemmer for serving on my committee as well as Dr. Charles “Ed” Harris for attending the defense. I enrolled in Dr. Harris’s *Ethics and Engineering* course as a senior undergraduate student and have served as a teaching assistant for the course for four semesters under Dr. Harris’s supervision, and his discussions have certainly contributed to my education.

I owe my utmost gratitude to my parents, James & Laurel Nudo, who have made great sacrifices to ensure the wellbeing of their children. My father has spent many nights on the road and across the world in a highly stressful sales career to ensure that each of his children graduates from college without debt. My mother has sacrificed by

not only working to assist her children financially, but also ensuring her children never returned to college after a visit home on an empty stomach, among countless other deeds that can never be adequately described in words.

My grandparents, Joseph & Eileen Nudo and Leon & Norma LoBello, wholeheartedly contributed to my education, demeanor, and spirituality. They each indicated their desire for me to complete higher education because they each had the desire to attend college but most were unable for financial considerations.

Finally, I would like to thank the members of the Surface Science laboratory in the department of mechanical engineering at Texas A&M University. I would especially like to thank Dr. Ke Wang, Dr. Subrata Kundu, Dr. Feng Gao, Dr. Gang Liang, Rodrigo Cooper, David Huitink, Michael Chiu, Brady Barkley, and Sukbae Joo.

NOMENCLATURE

Au	Gold
C	Carbon
Pd	Palladium
PVDF	Polyvinylidene fluoride
XPS	X-ray photoelectron spectroscopy

TABLE OF CONTENTS

Page

CHAPTER

LIST OF FIGURES

Page

CHAPTER I

INTRODUCTION

This chapter reviews a broad spectrum of topics from the materials science realm that are foundations for the present research. It starts with problems concerning failure of materials, followed by an introduction to the coupling of material properties, material bonding characteristics, mechanical properties, deformable bodies and stress analysis, XPS of thin-films, as well as hardness. Fundamental information concerning mechanical characterization was introduced in order to help readers to understand the results that indicate a relation between these mechanical phenomena to other properties.

1.1. Failure of Materials

In real world engineering applications, parts and structures fail from various loading schemes. To discover the failure method, it is necessary to study materials involved in the structure and the failure mechanisms. Yielding occurs due to plastic deformation caused by large stresses. Fracture occurs when a combination of applied stress and flaw size becomes too large, as denoted by $\sigma_f\sqrt{\pi c_{crit}} \geq \sqrt{2\gamma Y}$, where σ_f is the fracture stress, c_{crit} is the length of crack, γ is the intrinsic surface energy, and Y is Young's modulus [1]. Fatigue causes failure due to cyclic loading, and this loading is smaller than the material's tensile strength and often the yield strength as well [2].

This thesis follows the style of Thin Solid Films.

Creep failure is associated with stresses that cause materials to fail over long time periods even though the stresses may be less than the yield strength. High temperatures accelerate the problem [3]. Buckling is a failure mechanism that causes materials to fail in compression at stresses less than the compressive strength [4]. It is possible to calculate the force necessary to cause a beam to buckle with knowledge of the beam's support arrangement, area moment of inertia, length, and the material's modulus of elasticity. Rapid temperature change, otherwise known as thermal shock, causes materials to fail [5] via thermally-induced cracking.

All of these failure mechanisms are dependent upon the particular materials and their service environments involved. These materials are characterized by numerous properties: mechanical, electrical, optical, magnetic, thermal, chemical, acoustic, among others. It is necessary to study the development of these material properties from as small of a scale as possible. Manipulating materials at small length scales may lead to changes in the bulk material properties that prevent failure.

Likewise, it is necessary to corroborate the links between some of the aforementioned properties. For instance, piezoelectric materials experience a coupling effect between mechanical and electrical properties that allow them to be easily implemented in sensor technologies. Polyvinylidene fluoride (PVDF) is a polymer that has exhibited piezoelectric properties suitable for sensing devices and is utilized as a substrate for thin-film growth in this report. It is these materials' importance that exhibit couplings of various properties that leads to the necessity to study mechanochemistry, which is discussed in this chapter.

1.2. Coupling of Material Properties

Mechanochemistry is an ever-emerging field that involves the coupling between chemistry and mechanical phenomena. Its significance is rapidly increasing due to its applicability to engineering problems at small length scales. For instance, whereas in the past great engineering feats were often described at the macroscopic level like the construction of the Empire State Building and the National Aeronautics and Space Administration endeavors into space, today some of the greatest technologies are developed at much smaller length scales. Certainly nanoscale technological development requires intimate knowledge of the fundamentals of mechanochemistry due to the unique forces that exist at small length scales.

Throughout two millennia, the fundamentals of mechanochemistry have allowed scientists and engineers to explain many physical phenomena. Aristotle's student Theophrastus of Ephesus wrote an early text in the area of mechanochemistry concerning a mechanically activated chemical reaction that produces metallic mercury [6]. Mechanochemistry even has important consequences in the muscle of the human body [7]. Mechanochemistry also has implications at the material's surface. The surface of the material is important to materials scientists and engineers because the surface of the material exhibits different properties than the bulk of the material. This is especially important in nanoscale studies because nanoparticles often maintain relatively high surface area to volume ratios. There have been methods developed to produce nanoparticles from mechanochemical means [8]. Furthermore, the surface is extremely important when studying the chemical reactions of solids. Whereas heat-activated solid surfaces activate all lattice sites, mechanically activated solids may only activate portions of the lattice sites [9]. Solids are unique because unlike liquids and gases, they are capable to sustain shear strain, and shear strain provides a greater susceptibility to reactions due to the change in symmetry [10].

Mechanically-induced reactions may also have direct implications in technological development. For instance, mechanochemical reactions have been designed to produce carbon nanotubols [11]. Chemists have applied this study to the development of self-healing polymers and molecular strain gauges [12]. Mechanochemical fabrication has been employed in the creation of lead zirconate titanate [13]. Mechanochemistry is also essential for molecular motor development [14].

It is also possible to characterize chemical bonding from a mechanochemical analysis. In fact, mechanical strain may be developed to break a chemical bond. Developments in atomic force microscopy (AFM) allow for the development of force versus extension curves at much smaller length scales than typical stress-strain data achieved with a tensile and compressive test machine [15]. It is interesting to note that fluctuations in anodic polarization due to changes in plastic deformation have been termed the mechanochemical effect [16].

There are various mechanochemical processing methods including mechanical alloying, mechanical milling, and reaction milling [17]. Mechanical alloying involves the production of homogeneous materials from mixtures of elemental powders [18].

1.3. Materials and Bonding Structures

In order to understand material behavior small length scales, it is necessary to understand the bonds that hold them together. There are principally two types of bonding that will be considered: primary and secondary. The three forms of primary bonding that will be discussed are covalent, ionic, and metallic. The two forms of secondary bonding that will be discussed are hydrogen bonding and van der Waals bonding.

1.3.1. Primary

It is necessary to study primary bonds because the characteristics of these bonds give rise to bulk material properties such as Young's modulus and melting temperature.

1.3.1.1. Covalent

As a consequence of quantum mechanics, electrons align into shells and subshells. One such subshell is the *p* subshell displayed in Figure 1. The red lobes indicate the electron probability distribution, and the black sphere represents the nucleus. Because chemical bonding occurs between electron clouds, the *p* subshell in some cases may combine with the *p* subshell of another atom to form the σ molecular orbital that is displayed in Figure 2. The important characteristic of the σ molecular orbital is that there are no nodal planes, or planes with zero electron density, on the internuclear axis [19]. A σ bond, the strongest covalent bond, forms when the σ molecular orbital is filled with two electrons [19].

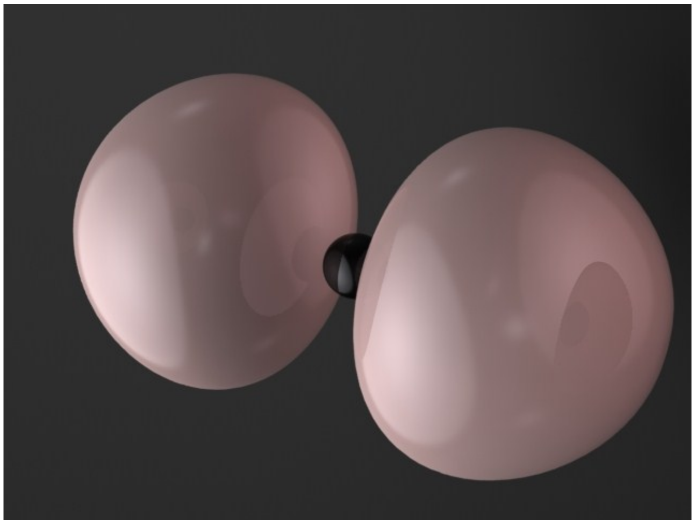

Figure 1. A *p* subshell contains two lobes indicating the electron probability distribution.

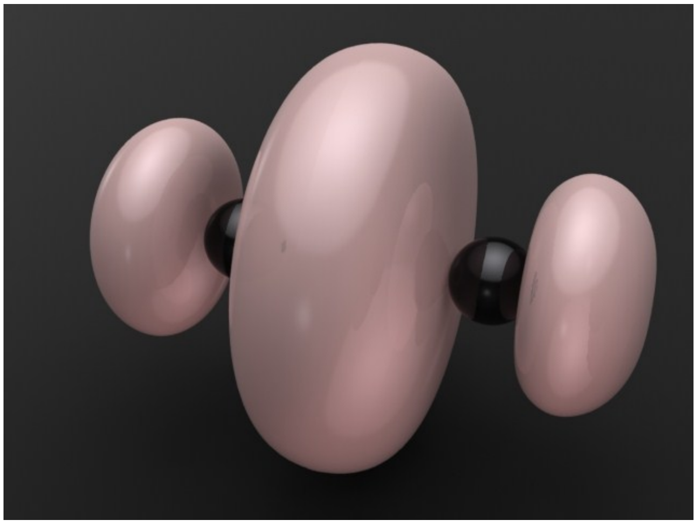

Figure 2. Two *p* subshells combine to form a σ molecular orbital.

Subsequently, the *p* subshells of two atoms may combine in an alternative manner as indicated in Figure 3, and this scenario is labeled a π molecular orbital. Notice that the π molecular orbital contains one nodal plane on the internuclear axis.

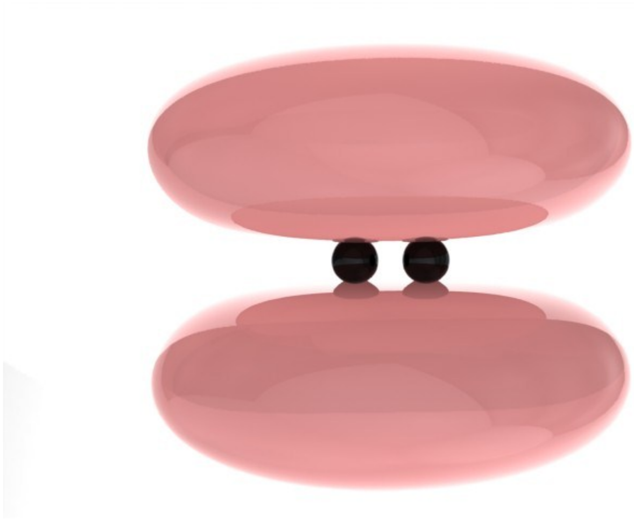

Figure 3. Two *p* subshells combine to form a π molecular orbital.

A π bond forms when two electrons inhabit the π molecular orbital, and in general, bonds formed via π bonds are weaker than σ bonds [19]. Finally, the *d* subshell is provided in Figure 4, and a *d* subshell is unique in the sense that it has the ability to form two nodal planes on the internuclear axis. This scenario, as indicated in Figure 5, is labeled a δ molecular orbital.

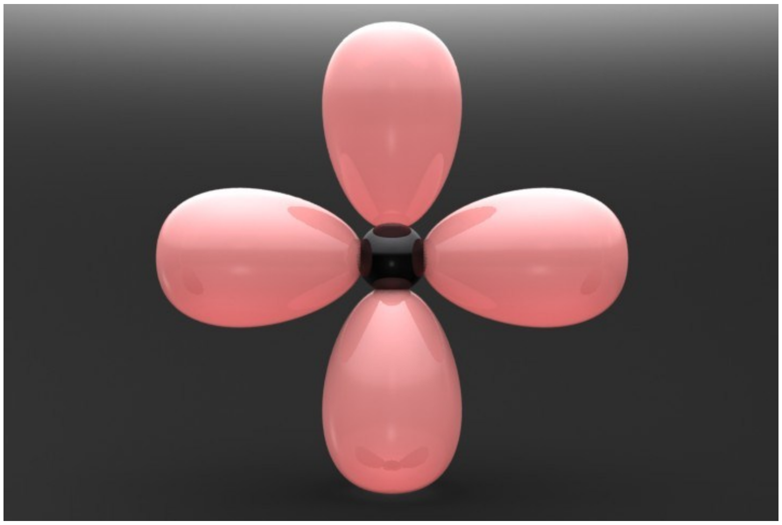

Figure 4. A *d* subshell contains four lobes indicating the electron probability distribution.

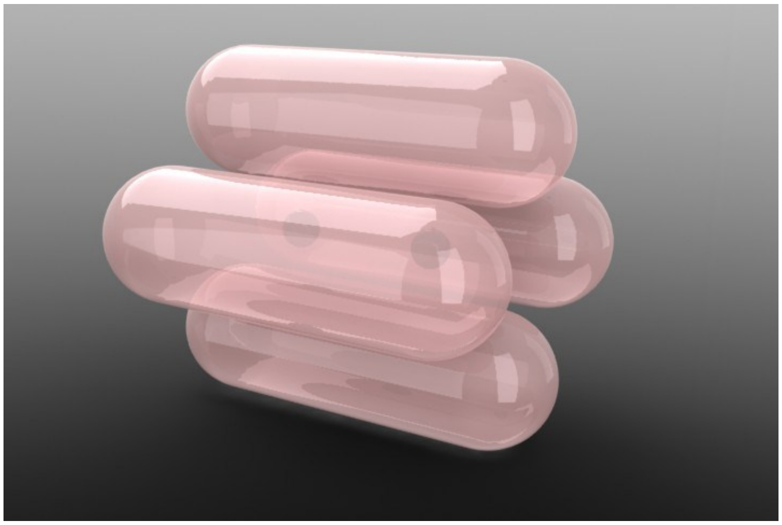

Figure 5. Two *d* subshells combines to form a δ molecular orbital.

1.3.1.2. Ionic

Ionic bonding is best described as the bond that occurs from the donation of electrons from one atom to another. In general, an electropositive atom donates electrons to an electronegative atom. For instance, sodium chloride, NaCl, maintains ionic bonds between sodium, an electropositive element, and chlorine, an electronegative element.

1.3.1.3. Metallic

Metallic bonds involve positive ions amidst a sea of electrons and occur between the metallic elements. Electrical conductivity is enhanced through metallic bonding because the electrons are not localized to any specific nucleus. In the presence of an electric field, the electrons in a metallically-bonded solid are capable of flowing, thus causing a current.

1.3.2. Secondary

Secondary bonds are in general much weaker than their primary bonding counterparts. The two types of secondary bonds that will be discussed in this report are hydrogen bonding and van der Waals bonding.

1.3.2.1. Hydrogen Bonding

A hydrogen bond exists between hydrogen attracted to an electronegative atom even though the hydrogen atom and the corresponding electronegative atom are already primarily bonded to other atoms. Although hydrogen is primarily bonded to oxygen in water (H_2O) and nitrogen is primarily bonded to hydrogen in ammonia (NH_3), if a molecule of water is in close proximity to a molecule of ammonia, the hydrogen atom of the water bond can be attracted to the nitrogen atom of the ammonia bond. This attraction leads to hydrogen bonding, and it is understandable why this type of bond is significantly weaker than primary bonding.

1.3.2.2. Van der Waals Bonding

Because electrons are continuously moving, the spatial charge distribution in a molecule is not a constant. Therefore, it is possible for a dipole to exist in a molecule in which a portion of the molecule is more positively charged and the other portion is more negatively charged. If this occurs in multiple molecules in close proximity at the same time, then this gives rise to van der Waals bonds due the negatively charged portion of one molecule will be attracted to the positively charged portion of another molecule in close proximity. It is also understandable why van der Waals bonding is much weaker than primary bonding.

1.4. Mechanical Properties

The aforementioned bonding types lead to the mechanical properties that determine how materials behave under stress and ultimately determine if a material fails. Yield strength is the strength at which plastic deformation begins to occur. Tensile strength is the maximum engineering stress that a material undergoes before failure. Young' modulus, or modulus of elasticity, is a quantity that describes the slope of the initial elastic region of the stress and strain curve. It is interconnected to the material stiffness, which is the slope of the force versus interatomic separation curve at zero force. Finally, Poisson's ratio relates longitudinal strain to transverse strains.

1.5. Deformable Bodies and Stress Analysis

1.5.1. Strain

Strain is best defined through the relative changes in position among material points in a solid body. As indicated in Figure 6, points P_A and P_B, which are initially separated by an infinitesimally small vector $d\vec{r}$, move to positions $P_A^{'}$ and $P_B^{'}$ upon deformation, respectively.

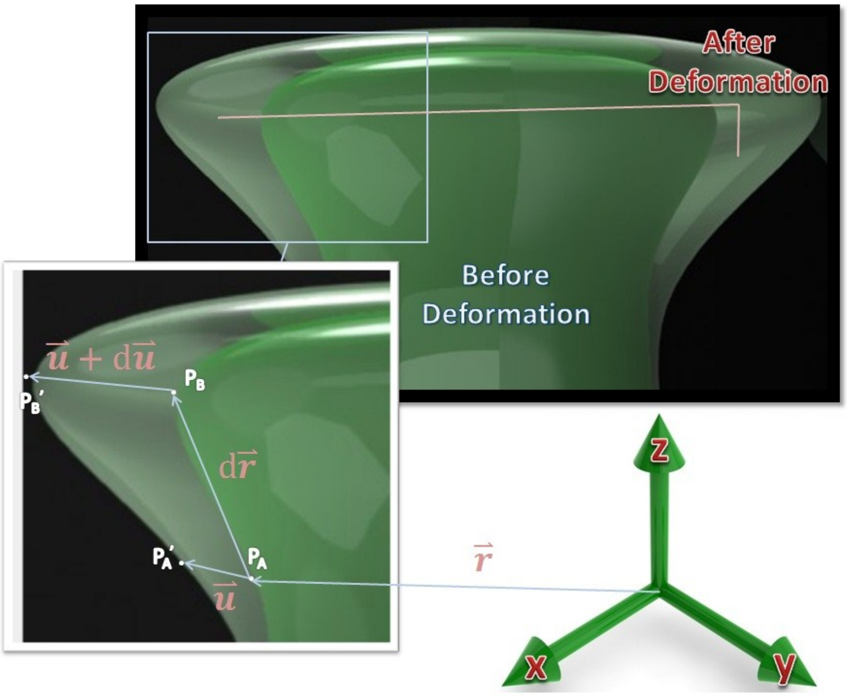

Figure 6. The figure displays a method to describe deformations as rigorously defined in elasticity studies.

It is necessary to define these vectors in mathematical terms. First, the point P_A is initially located at $\vec{\boldsymbol{r}} = \begin{bmatrix} x \\ y \\ z \end{bmatrix}$. Next, the infinitesimally small vector that separates points P_A and P_B is $d\vec{\boldsymbol{r}} = \begin{bmatrix} dx \\ dy \\ dz \end{bmatrix}$ [20]. The P_A displacement vector is defined as $\vec{\boldsymbol{u}} = \begin{bmatrix} u_x \\ u_y \\ u_z \end{bmatrix}$ [20]. Likewise, the P_B displacement is demarcated as the sum of the P_A displacement and the infinitesimally small differential vector $d\vec{\boldsymbol{u}} = \begin{bmatrix} du_x \\ du_y \\ du_z \end{bmatrix}$ [20]. It is necessary to realize that the differential of an arbitrary quantity *w* is defined in three dimensions as $dw = \frac{\partial w}{\partial x} dx + \frac{\partial w}{\partial y} dy + \frac{\partial w}{\partial z} dz$ [21]. Therefore, it follows that $d\vec{\boldsymbol{u}}$ may be described in the following terms [20].

$$du_x = \frac{\partial u_x}{\partial x} dx + \frac{\partial u_x}{\partial y} dy + \frac{\partial u_x}{\partial z} dz$$

$$du_y = \frac{\partial u_y}{\partial x} dx + \frac{\partial u_y}{\partial y} dy + \frac{\partial u_y}{\partial z} dz$$

$$du_x = \frac{\partial u_z}{\partial x} dx + \frac{\partial u_z}{\partial y} dy + \frac{\partial u_z}{\partial z} dz$$

This scenario may be rewritten as $d\vec{\boldsymbol{u}} = \begin{bmatrix} \frac{\partial \mathrm{u_x}}{\partial \mathrm{x}} & \frac{\partial \mathrm{u_x}}{\partial \mathrm{y}} & \frac{\partial \mathrm{u_x}}{\partial \mathrm{z}} \\ \frac{\partial \mathrm{u_y}}{\partial \mathrm{x}} & \frac{\partial \mathrm{u_y}}{\partial \mathrm{y}} & \frac{\partial \mathrm{u_y}}{\partial \mathrm{z}} \\ \frac{\partial \mathrm{u_z}}{\partial \mathrm{x}} & \frac{\partial \mathrm{u_z}}{\partial \mathrm{y}} & \frac{\partial \mathrm{u_z}}{\partial \mathrm{z}} \end{bmatrix} \begin{bmatrix} dx \\ dy \\ dz \end{bmatrix} = \varepsilon d\vec{\boldsymbol{r}}$ [20],

where $\varepsilon = \begin{bmatrix} \frac{\partial \mathrm{u_x}}{\partial \mathrm{x}} & \frac{\partial \mathrm{u_x}}{\partial \mathrm{y}} & \frac{\partial \mathrm{u_x}}{\partial \mathrm{z}} \\ \frac{\partial \mathrm{u_y}}{\partial \mathrm{x}} & \frac{\partial \mathrm{u_y}}{\partial \mathrm{y}} & \frac{\partial \mathrm{u_y}}{\partial \mathrm{z}} \\ \frac{\partial \mathrm{u_z}}{\partial \mathrm{x}} & \frac{\partial \mathrm{u_z}}{\partial \mathrm{y}} & \frac{\partial \mathrm{u_z}}{\partial \mathrm{z}} \end{bmatrix}$ [20]. The strain matrix e is defined as $e = \frac{1}{2}(\varepsilon + \varepsilon^T)$ [20].

The definition for strain can be expanded to matrix form as

$e = \begin{bmatrix} \frac{\partial u_x}{\partial x} & \frac{1}{2}\left(\frac{\partial u_x}{\partial y} + \frac{\partial u_y}{\partial x}\right) & \frac{1}{2}\left(\frac{\partial u_x}{\partial z} + \frac{\partial u_z}{\partial x}\right) \\ \frac{1}{2}\left(\frac{\partial u_x}{\partial y} + \frac{\partial u_y}{\partial x}\right) & \frac{\partial u_y}{\partial y} & \frac{1}{2}\left(\frac{\partial u_y}{\partial z} + \frac{\partial u_z}{\partial x}\right) \\ \frac{1}{2}\left(\frac{\partial u_x}{\partial z} + \frac{\partial u_z}{\partial x}\right) & \frac{1}{2}\left(\frac{\partial u_y}{\partial z} + \frac{\partial u_z}{\partial x}\right) & \frac{\partial u_z}{\partial z} \end{bmatrix}$. This is rewritten in simpler notation as $e = \begin{bmatrix} \varepsilon_{xx} & \frac{1}{2}\gamma_{xy} & \frac{1}{2}\gamma_{xz} \\ \frac{1}{2}\gamma_{xy} & \varepsilon_{yy} & \frac{1}{2}\gamma_{yz} \\ \frac{1}{2}\gamma_{xz} & \frac{1}{2}\gamma_{yz} & \varepsilon_{zz} \end{bmatrix}$ where ε_{xx}, ε_{yy}, and ε_{zz} are normal strains and γ_{xy}, γ_{xz}, and γ_{yz} are shear strains [20]. Normal strains indicate changes in distances between material points after deformation whereas shear strains correspond to changes in angles between material points.

It should be noted that the relatively large deformation associated with Figure 6 may in actuality be more indicative of large deformation theory as opposed to small deformation theory; however, an exaggeration has been created between the two states for viewing purposes and clarity. Finally, it is necessary to understand the approach that was presented to quantify strain is maintained by a Cartesian coordinate system. In numerous cases it is more appropriate to employ curvilinear coordinate systems, such as cylindrical and spherical coordinate systems, in order to simplify the calculations.

1.5.2. Stress

Material points may be exposed to either body forces or surface forces. Body forces are exerted on all particles within the body and arise due to gravity, magnetism, and other causes. Surface forces are exerted along the boundary of the body and its surroundings. The forces acting on the body may either be relatively simple or complex; however, it is always useful to develop a stress cube for deformable body analysis as shown in Figure 7.

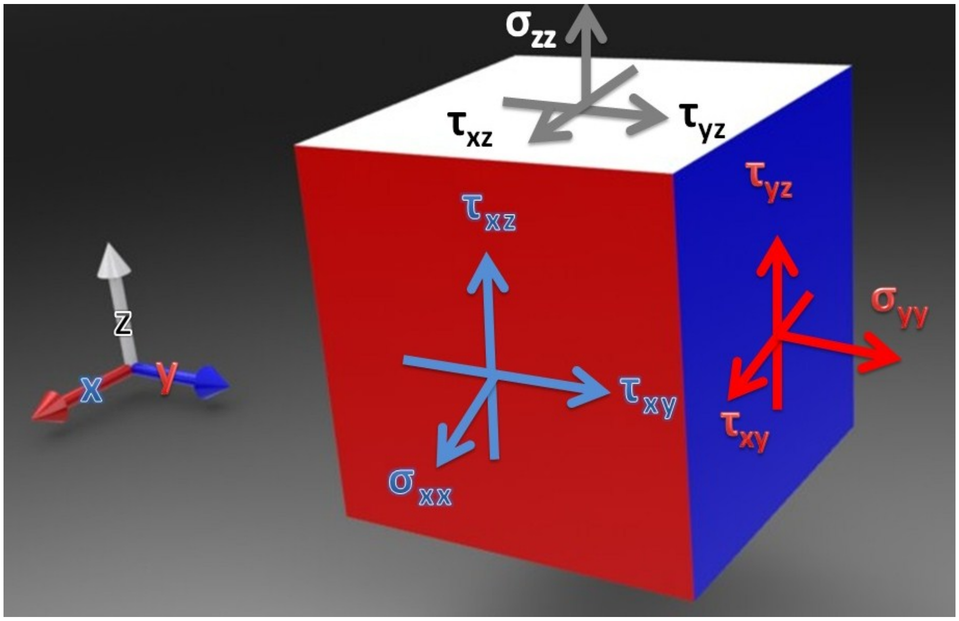

Figure 7. A stress cube is a useful tool in the analysis of deformable bodies.

The stress cube represents a specific material particle within the deformable body. When using Cartesian coordinates, the positive *x*, *y*, and *z* faces are defined as those faces located on the stress cube that share the *x*, *y*, and *z* coordinate axes, respectively, as normal vectors. On these faces, normal stresses are indicated by σ and shear stresses are indicated by τ. Each stress also maintains two subscripts. While the first subscript specifies the face upon which the stress is located, the final subscript signifies the direction along which the stress acts on the stress cube. Therefore, when both subscripts of a particular stress are the same, this indicates a normal stress because normal stresses act along the faces' normal vectors. Likewise, when the subscripts of a particular stress are not the same, this indicates a shear stress because shear stresses act perpendicular to the faces' normal vectors. In Figure 7, τ_{yx} and τ_{zy} have been relabeled τ_{xy} and τ_{yz}, respectively, because in order for the summation of moments acting on the stress cube to be zero, it is required that τ_{xy} and τ_{yx} are equal as well as τ_{yz} and τ_{zy} are equal.

1.6. XPS of Thin-Films

Because the research presented in this report is largely based in the X-ray photoelectron spectroscopy study of thin-films, it is necessary to review previous significant results in this field by other researchers. Sasha and Tompkins report the use of XPS to study the oxidation of titanium nitride thin-films [22]. In this research, titanium nitride films were deposited via reactive sputtering to produce 350 nm titanium nitride films. After an oxidation procedure and annealing, the samples were analyzed with XPS using Mg Kα X-rays. The researchers suggest that the film changes from an amorphous film to a crystalline film.

Shallenberger, Cole, and Novak report the use of XPS to characterize silicon oxynitride thin-films [23]. They discuss the translation of the $N(-Si)_3$ peak by oxygen atoms as well provide insight into nitrogen areal density as determined by XPS. XPS will be later used in this research to demonstrate a connection between changes in electron binding energy to applied strain.

1.7. Hardness

In general, hardness is a measure of the resistance to permanent deformation and is estimated by the relationship between the permanent indentation area formed on a sample material's surface by an indenter and the indenter load. Hardness testing has its origins from scratch testing by Reaumur in 1722 and the Mohs scale of hardness in 1822 [24]. The Brinell test, introduced by Johann Brinell to the Swedish Society of Technologists over one hundred years ago, involves a spherical indenter penetrating a sample material surface [24]. This development was followed in 1919 by the Rockwell test and has revolutionized the field of hardness testing [24].

Nanotechnology is an emerging multidisciplinary field that has the potential to radically transform existing technologies and develop new tools and systems to exponentially improve both knowledge and standard of living. Therefore, it is essential to develop testing techniques that measure, in length scales of less than 100 nm, the quantities typically associated with macroscopic dimensions. Recent developments in nanoindentation have allowed engineers and scientists to estimate hardness at much smaller length scales than the limitations provided by Brinell, Rockwell, and other conventional hardness tests.

1.7.1. Brinell Hardness

Although not measured in this work, it is important to understand macroscopic hardness tests, like the Brinell hardness, before introducing nanoindentation. This test involves a spherical indenter puncturing the surface of the test material. A load, *L* (in kilograms), forces a sphere of diameter *D* (in millimeters) into the surface of a material, creating a crater with diameter *d* (in millimeters). The diameter *d* is calculated as the average of two measured perpendicular diameters [24]. The equation below defines the hardness, HB, in terms of the previously defined quantities [24]:

$$\boldsymbol{HB = \frac{L}{\frac{\pi D}{2}\left(D - \sqrt{D^2 - d^2}\right)}}$$

In this equation, the denominator represents the indentation surface area [25], so the measurement is the ratio of load to indentation surface area. Likewise, Figure 8 displays a schematic that pictorially describes the Brinell hardness testing theory.

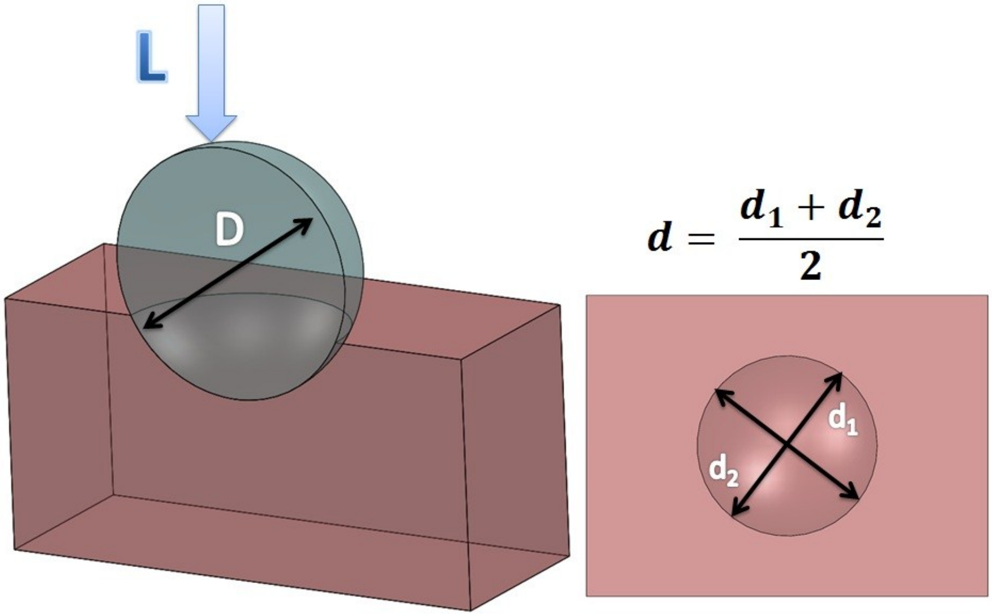

Figure 8. The figure displays the theory associated with Brinell hardness measurements. A load, *L*, is applied to a spherical indenter with diameter *D*, and the indentation diameter, *d*, is subsequently measured.

The sphere is typically tungsten carbide or hardened steel 10-mm diameter ball inserted into the material surface with a load that ranges from 500 to 3000 kg [24]. It is important to use a sample that is thick enough so that only the top surface is affected by the indentation and to also avoid areas close to the sample's edges [26].

CHAPTER II

MOTIVATION AND OBJECTIVES

There is a general desire in the scientific community to better estimate material properties at small length scales. For instance, at the macroscopic level there are numerous material properties published in textbooks and papers that scientists and engineers often take for granted. When designing a bridge, a civil engineer may employ quantities like yield strength and modulus of elasticity in order to confirm that the bridge does not fail. The engineer may decide to use textbook values or perform standardized tests to measure these quantities. Likewise, an engineer designing a nanomachine may also need these quantities as well. Unfortunately, it is an exceedingly more difficult task to search for a database of modulus of elasticity and yield strength values between two atoms in comparison for a bulk material; therefore, it is necessary to develop testing techniques that allow for large-scale testing of these quantities.

Of course, Lennard-Jones parameters exist to estimate the potential energy and forces that exist between two atoms. In fact, the derivative of the interatomic force as a function of distance between two atoms may represent a decent estimate of the modulus of elasticity between two atoms. Unfortunately, these Lennard-Jones parameters are often the subject of numerical techniques and computer simulations to estimate potential energies as functions of interatomic distance; therefore, these quantities' accuracy is understandably questionable. Returning to the example of the civil engineer designing a bridge, it is highly unlikely that he will use a modulus of elasticity value for carbon steel that has been estimated by a computer. Furthermore, if the engineer is designing a bridge with a particular heat treatment of steel, it is doubtful that a computer simulation will accurately model the intricacies of such a material system. The engineers should find multiple sources for the specific heat treatment of steel to verify the quantity before implementing the design. Furthermore, if funding is available, the engineer is best suited to measure these quantities because laboratory testing will produce more reliable results than data obtained from a textbook. Likewise, engineers who work at the nanoscale deserve nothing less than the exquisite material property databases available to engineers who work at the macroscopic scale as well as similar testing techniques.

It is the objective of this research to establish the relationship between induced strain in thin-films to a shift in electron binding energy, which is an electrical property, to the area beneath the load-displacement indentation curve. Both quantities are forms of energy. This thesis will demonstrate the direct connection between strain and the energy required to free core-level electrons from atoms. Of course the mechanical strain induces a stretch in the bonds. Furthermore, the energy required to free core-level electrons from atoms, or the core-level binding energies, is related to the interatomic force between two atoms.

Once the objective is achieved, the relationship between electron binding energy and strain may be utilized in unique sensing devices. For instance, it is desired to estimate the strain in a nanogear. With knowledge of the fluctuation of the electron binding energy of the constituent atoms with strain, it may be possible to estimate the strain in such a small device.

CHAPTER III

EXPERIMENTAL PROCEDURE

As mentioned in Chapter II, Motivation and Objectives, this research investigates relationships between mechanical strain and electronic binding energy. Experimental approaches are proposed to detect, characterize, and evaluate mechanical, physical, and spectroscopic properties of selected materials. This chapter comprises four topics. It begins with the material, their selection and properties, sample preparation, XPS procedure, and finally concludes with the nanoindentation procedure.

XPS is discussed to highlight its capability to measure electron binding energy. Next, hardness testing is explained in detail. Although the thesis involves nanoindentation measurements, Brinell and Vickers hardness tests are first presented so that the macroscopic techniques are understood before mastering the hardness testing methods designed for much smaller length scales.

3.1. Materials

Gold (Au) and Palladium (Pd) were chosen to study for a multitude of reasons. First, gold is a malleable and ductile metal that is relatively inert to the surrounding environment [27]. Next, gold has many applicable industrial applications. For instance, it is often applied to the surfaces of metals as a coating for corrosion resistance and is often used in conjunction with nickel [27]. Of course, gold has numerous applications outside of industrial applications, like jewelry and currency.

Palladium is often developed as a thin-film for instrument mirror plating due to its reflectivity [27]. Mixtures of gold and palladium are often employed in dental applications, and gold-palladium alloys are utilized in electrical industries due to their electrical conductivity [27]. Furthermore, mixtures of gold and palladium are manufactured as targets for the sputter coating deposition process, and this allows easy implementation into the present study. Table 1 provides a summary of significant material properties of gold and palladium.

Table 1.
Significant material properties of gold and palladium are provided in the table.

Property	Gold (Au)	Palladium (Pd)
Melting Temperature (K)	1337 [28]	1826 [29]
Density (g/cm^3)	19.30 [30]	11.78 [31]
Poisson's Ratio	0.33 [32]	0.35 [33]
Young's Modulus (GPa)	77 [34]	120 [27]
Tensile Strength (MPa—annealed)	120 [27]	230 [27]
Hardness (Mohs—scratch)	2.5—3 [27]	4.5—5 [27]
Specific Heat (cal/g)	0.0312 [27]	0.058 [27]
Thermal Conductance (cal/sec)(cm^2)(°C/cm)	0.743 [27]	0.18 [27]
First Ionization Potential (eV)	9.223 [27]	8.33 [27]
Electronegativity (Pauling)	2.4 [27]	2.2 [27]

3.2. Thin-Films

Thin-films are an emerging technology that has the prospect to revolutionize current and future technologies. In general, the surface properties of materials are dissimilar to the bulk properties. Because thin-films maintain greater surface area to volume ratios than their typical engineering material counterparts, the surface properties become significant in these materials. Mechanically, thin-films may be superior to standard engineering materials in particular applications. For instance, some thin-films maintain higher strengths than cold worked bulk materials and some have displayed strengths that are approximately 200 times greater than annealed bulk material counterparts [35]. Optically, thin-films have been used for antireflection coatings, reflectors, and filters [35]. Magnetically, thin-films are employed in computer memory [35]. Finally, thin-films are important for electronic applications such as resistors and capacitor electrodes [35].

Thin-films were developed in this research in order to provide the necessary stretch of the atomic bonds to make inferences about the nature of the atomic bond. Schematics of these thin-films are provided. Figure 9 displays the flat sample. Gold and palladium were sputtered on a thin-film of polyvinylidene fluoride (PVDF) that was attached to glass with double-sided carbon tape.

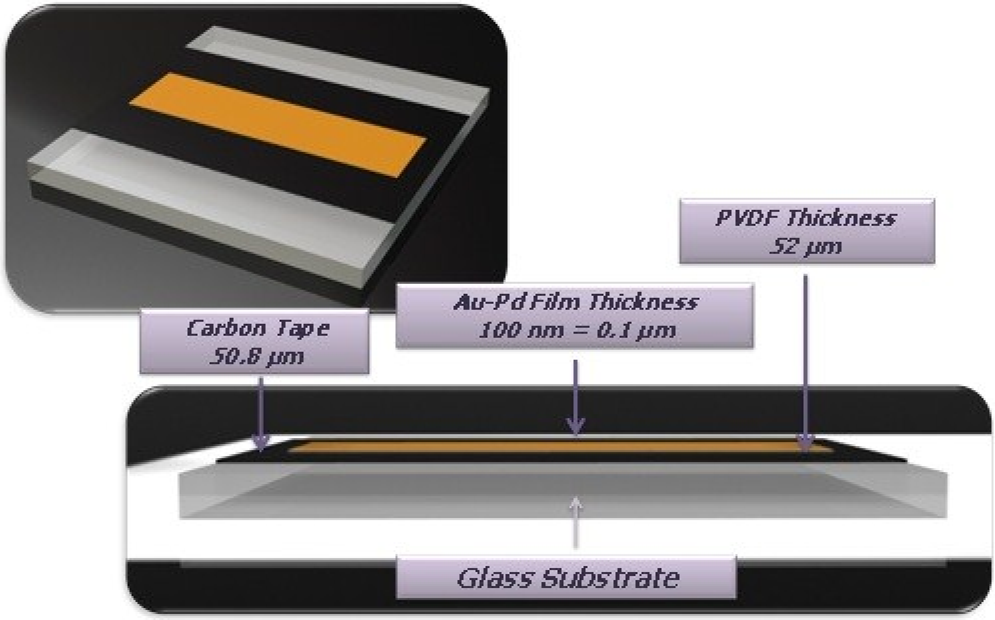

Figure 9. The figure displays the flat sample.

Figure 10 provides the schematic of the convex sample. The convex sample was produced in the same manner as the flat sample. The sample was stretched over the convex surface after the sputter deposition process.

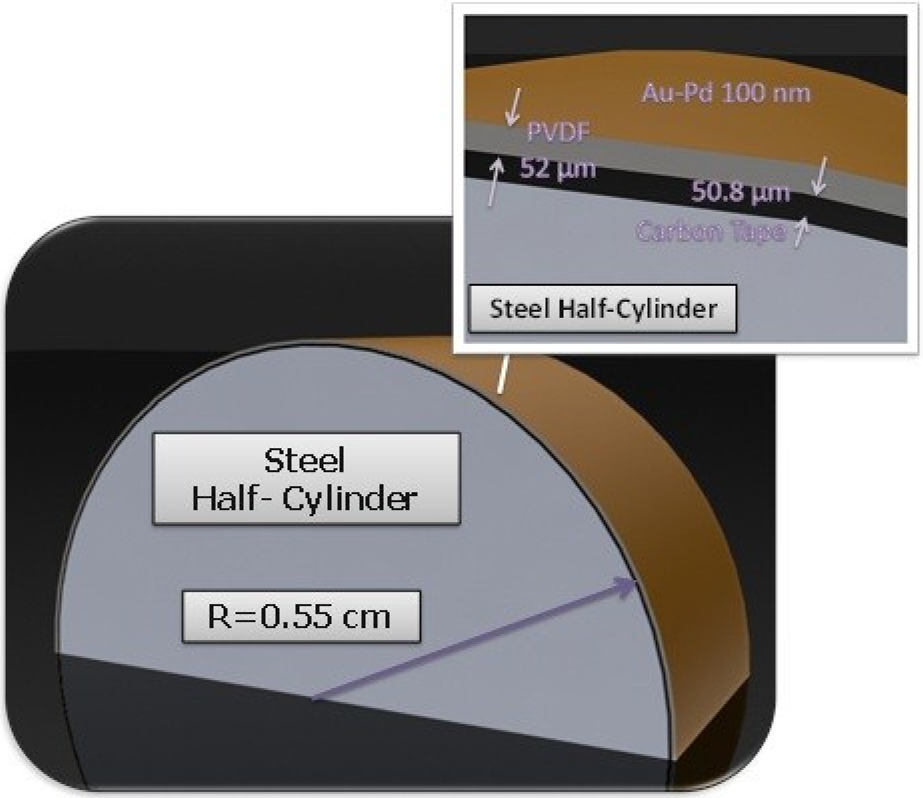

Figure 10. The figure displays the convex sample.

Figure 11 provides the concave sample. It was produced in the same fashion as the flat and convex samples. The sample was stretched over the concave surface after the sputter deposition process. Samples were also produced without the double-sided carbon tape, and evidence from the optical microscope suggests that these samples provided a more uniform microstructure. The optical microscope images are provided in the next chapter of this report.

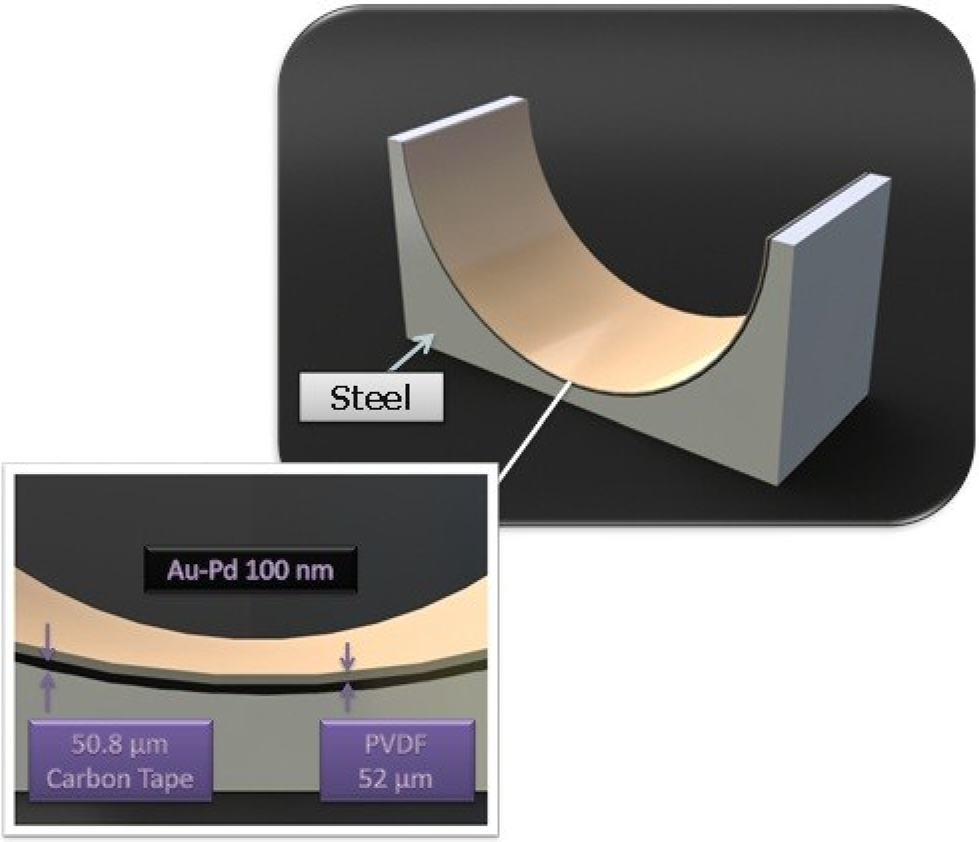

Figure 11. The figure displays the concave sample.

3.2.1. Thin-Film Deposition

Deposition technologies are essential to the microelectronics and semiconductor industries. For instance, unique methods are necessary for thin-film deposition for electronic components, electronic displays, coatings (optical, antistatic, and hard surface), and magnetic and optical data storage devices [36]. Thin-film deposition processes can be categorized as physical processes, chemical processes, or physical-chemical processes that combine aspects of both physical and chemical methods [36]. A brief introduction is provided below concerning common deposition techniques. Subsequently, the method employed specifically for this study is detailed.

3.2.1.1. Physical Vapor Deposition

3.2.1.1.1. Sputter Deposition

There are a variety of sputter deposition techniques; however, the planar diode sputter deposition is the focus of this research. In planar diode sputter deposition, a target material is bombarded by positively charged ions causing atoms from the target material surface to escape through the plasma onto the surface of a substrate. Electrons create cations by ionizing the gas in the chamber via collisions. The target material, the cathode, is connected to a negative potential and attracts the positively charged cations necessary for target bombardment. The target material deposits onto the substrate material, the anode. A disadvantage associated with planar diode sputter deposition is that the film that deposits on the substrate is heated throughout the process because the substrate attracts electrons [37]. Figure 12 provides a schematic of the sputter deposition technique.

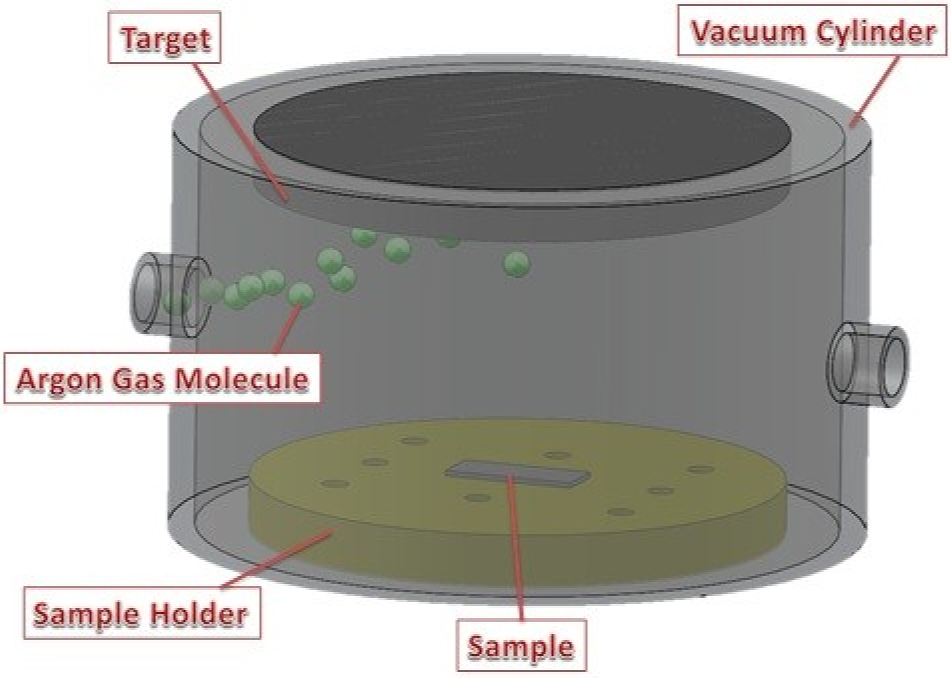

Figure 12. The figure displays the sputter deposition technique.

It is necessary to explain the target bombardment process in more detail. First, one may ask the question, “Why use ions to bombard the target?” In order to sputter individual atoms from the target material surface, it is necessary to use an object with atomic dimensions [36]. Because the sputtering technique is dependent upon momentum transfer, the ion must have enough momentum to transfer to the target surface atoms in order to initiate the release of atoms from the target surface. Electrons do not maintain enough momentum to fulfill this requirement [36]; however, the argon ions commonly used in sputter deposition maintain enough momentum to initiate this process. It is theoretically not required to use ions in sputter deposition; however, it is easier to accelerate charged particles in the presence of an electric field than neutral atoms [36]. Finally, noble gases are often used as the bombarding species due to their inertness to prevent chemical activity between the bombarding ions and the target material [36].

This thesis involves the sputter deposition of gold and palladium with approximately 100 nanometer thickness onto the surface of polyvinylidene fluoride (PVDF) with a thickness of approximately 52 μm as well as to the surface of aluminum foil and PVDF with a silver coating. The details of the process are provided in the subsequent paragraphs.

In the present research, the sputter deposition process was employed in order to create the thin-films. The Technics Hummer II sputter system was utilized with a gold and palladium target. The gold and palladium comprised the target, which acted as a cathode (negative potential) and was situated as the uppermost portion of the vacuum. The sample holder was placed directly across from the target. The current was held constant at 10 mA. The resulting thin-film thickness is a function of both sputtering time as well as current. Increasing sputtering time as well as increasing current both yield thicker thin-films. Figure 13 provides the resulting thin-film thickness for various times and currents.

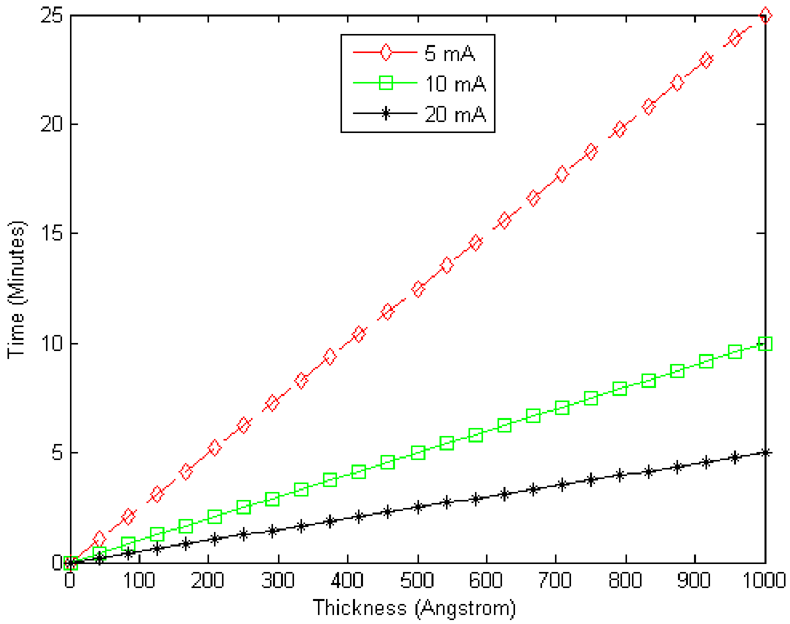

Figure 13. The figure displays the sputter deposition rates using the Technics Hummer II sputter coater with 5 mA, 10 mA, and 20 mA current.

The process was set in Auto mode instead of Manual mode so that the system automatically cycled on and off intermittently. The timer was set to ten minutes, and when the timer returned to zero, the timer was subsequently set to another ten minutes. Therefore, the total sputtering time was ten minutes. The sputtering occurred for only ten minutes due to the fact that the Auto mode cycles the power so that it sputters for half of the time. In other words, the sputtering process cycles intermittently throughout the entire procedure. The best procedure to follow in order to ensure a suitable vacuum was to allow the system to reach 300 mTorr before sputtering and then allow they system to remain at approximately 500 mTorr during the sputter deposition process. The system with exception to the argon tank is displayed in Figure 14 and a closer view of the target and sample holder is displayed in Figure 15.

In Figure 14, the high voltage control area of the system is displayed in the bottom right-hand portion of the figure. This area allows the user to turn on the high voltage as well as control the voltage. Moving clockwise, the ammeter is displayed. The ammeter allows the operator to determine the current. Next the timer is displayed and allows the user to control the amount of time the sputtering process occurs. The vacuum gauge is displayed so that the operator can determine the pressure within the chamber. Next, the target is displayed, which is the origin of the material that deposits on the sample. The sample holder is also displayed, and it holds the sample. Finally, the pressure control is displayed. The left knob allows the user to open and close the pressure control valve, and the right knob allows the operator to control the argon current.

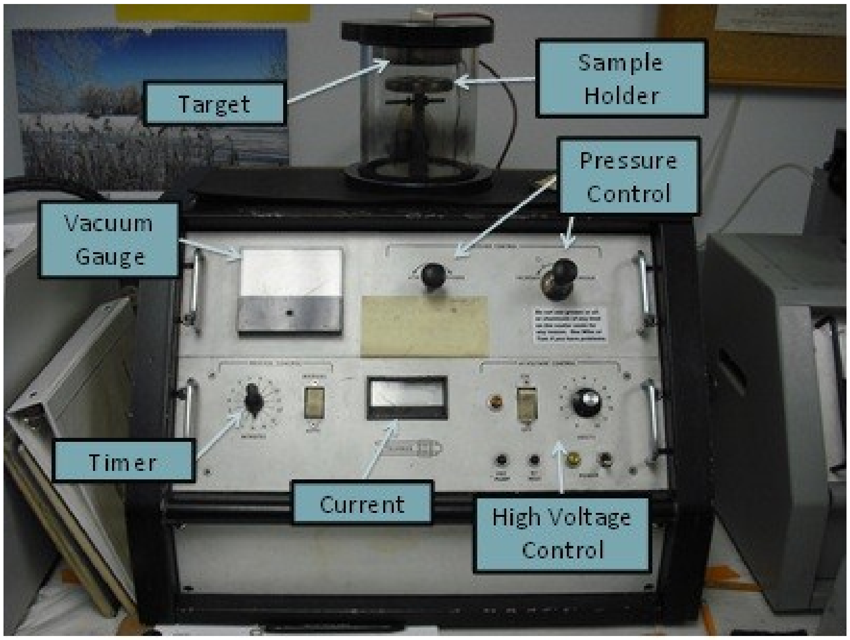

Figure 14. The sputter coating system is a Technics Hummer II.

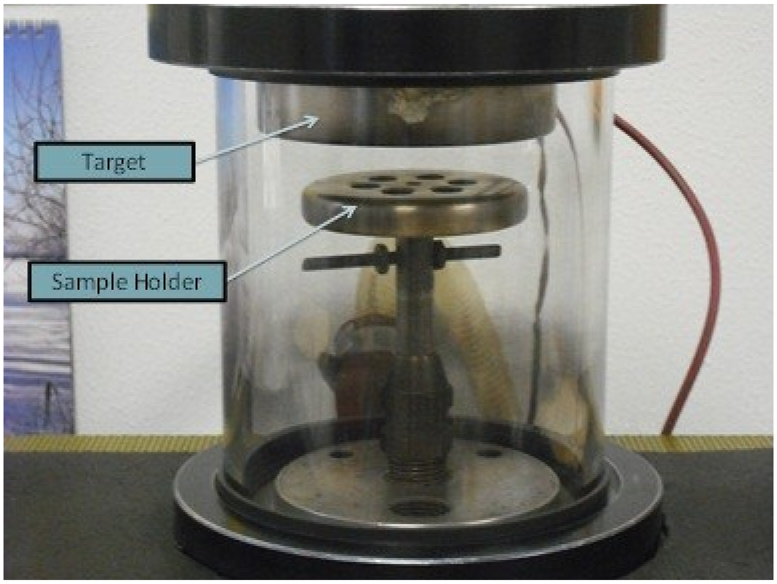

Figure 15. The target and sample holder are displayed.

3.2.1.1.2. Evaporation Deposition

Another common physical vapor deposition technique for thin-film development is the evaporation deposition process. In this process, a source material is evaporated within a crucible. The vapor produced from this process condenses on the substrate where the corresponding thin-film growth occurs [38]. Figure 16 provides a schematic of the evaporation deposition process.

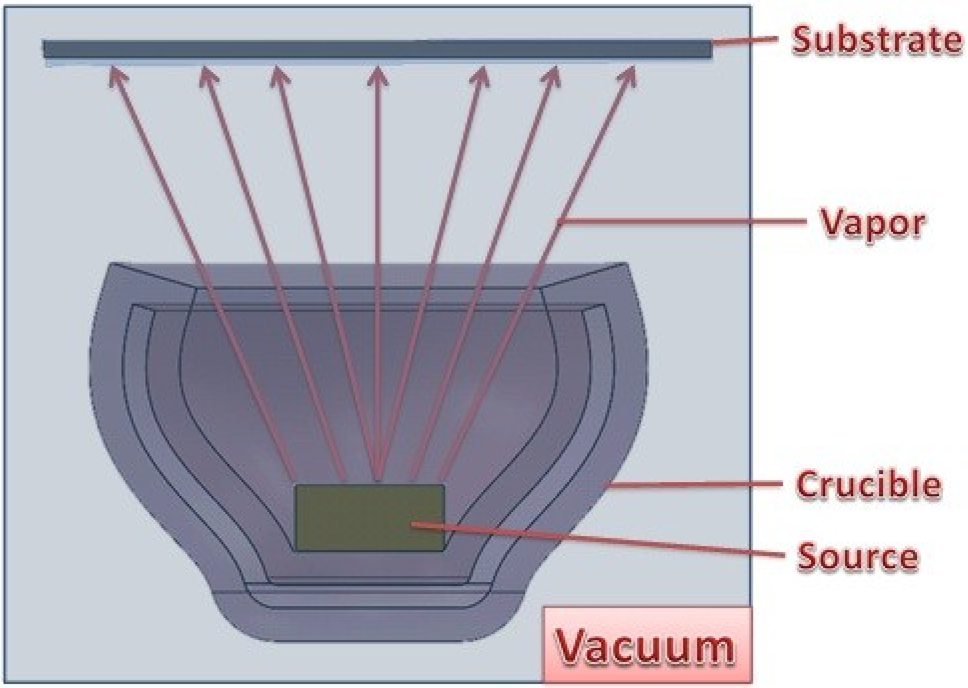

Figure 16. The evaporation deposition process is presented in the schematic.

3.3. XPS

XPS is a surface technique that exploits the photoelectric effect in order to measure electron binding energy. The binding energy represents a fundamental mechanical property of a material and is the mechanical work needed to pull a material apart. The binding energy measured using XPS is the energy required to remove core-level electrons from atoms in the material. It is related to the ionization energy, which is the energy required to remove the most weakly bound electron [39]. In XPS, photoelectrons are excited by the incident X-ray and are collected from the sample material's top 5 nm [40]. This means that the XPS is a powerful tool to analyze surfaces. As the sample material absorbs X-rays, a form of electromagnetic radiation, the sample material emits the photoelectrons whose kinetic energies are measured in the spectrometer.

The XPS contains three major components: an X-ray tube, detector, and analyzer. The X-ray tube produces electrons with an electron gun onto the surface of an aluminum or magnesium anode. The anode subsequently produces Kα characteristic X-rays which are directed onto the sample surface. A thin-film separates the X-ray tube and sample so that electrons do not escape from the X-ray tube into the sample chamber [40]. The photoelectric effect causes electrons to escape from the sample material surface. The analyzer subsequently measures the photoelectrons' kinetic energies. With knowledge of the spectrometer work function, energy of the x-ray, and the photoelectrons' kinetic energy, the photoelectrons' binding energy is subsequently calculated. A monochromatic beam of photoelectrons exits the analyzer and enters the detector that counts the number of photoelectrons at a particular kinetic energy. Finally, a plot is developed with the number of photoelectrons as a function of binding energy. Figure 17 displays a simplified schematic of this process.

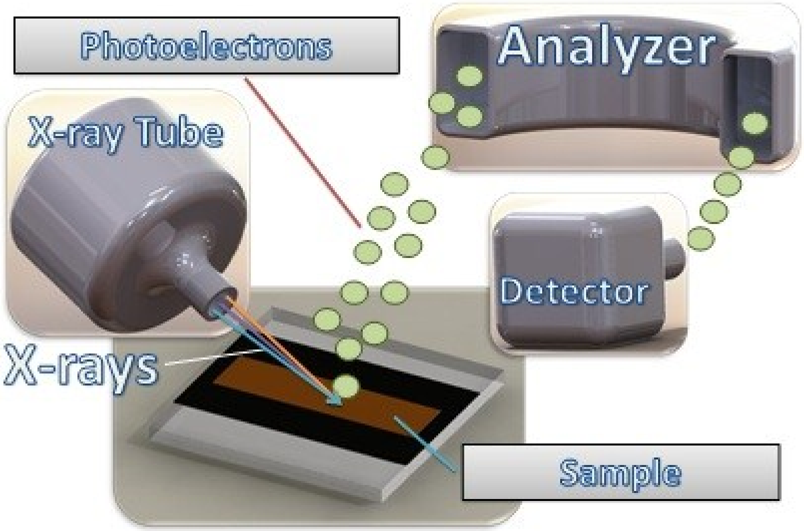

Figure 17. The figure displays a simplified schematic of the mechanisms involved with XPS. The relative sizes of the objects in the figure are exaggerated.

The Axis Ultra produced by Kratos Analytical was used for all X-ray photoelectron spectroscopy measurements. It incorporates a spherical mirror analyzer and an eight channel detector [41]. Because all tests were completed in spectrum mode, the analyzer functioned as a standard hemispherical analyzer [41].

A standard operating procedure is followed for samples tested with XPS. The electron binding energies were measured with high resolution scans of carbon, palladium, and gold. The carbon peak was measured for calibration purposes. The measured carbon peak for each sample was subtracted from 284.5 eV, typically considered to be a reliable value for the electron binding energy to the carbon-carbon bond. The difference between the standard and the measured electron binding energy for the carbon peak was added to the binding energies for the palladium and gold peaks.

In this research, the sample analysis chamber was set between 10^{-8} and 10^{-9} torr. The sample transfer chamber was initially set between 10^{-6} and 10^{-8} torr, but the pressure is increased in order to introduce the sample into the transfer chamber. The pass energy was set to 20. Each element of interest was scanned five to ten times in order to obtain an accurate measurement of the binding energy. The center of the carbon 1s peak was centered at 284.45 eV with a 23.1 eV width. The center of the palladium 3d peak was centered at 339.45 eV with a 20 eV width. The center of the gold 4f peak was centered at 86.45 eV with a 20 eV width.

3.4. Nanoindentation

Nanoindentation allows researchers to make connections and draw inferences between mechanical properties like Young's modulus and hardness to other conditions like morphology and processing techniques [42]. The research in this report concerns the link between Young's modulus and electron binding energy, which is a novel approach because it provides a connection between mechanical and electrical aspects of materials.

In this research, an MTS XP nanoindentation instrument was utilized to measure the samples' mechanical properties. A coil and magnet assembly applies the necessary load to the indenter. Subsequently, the displacement is measured via a capacitance gauge. The capacitance gauge is able to function as a displacement sensor because capacitance is inversely proportional to the distance between the capacitor plates through the equation $C = \frac{A\varepsilon}{d}$, where C is capacitance, A is the capacitor plate area, and ε is the dielectric permittivity.

3.5. Digital Microscope

The digital microscope used in this research is the Keyence VHX-600. It is equipped with a 15-inch LCD monitor and high resolution lenses capable of magnifications of up to 5000. Transmitting illumination was used by connecting the fiber optic cable into the corresponding transmitting illumination connector on the lens stand. An image of the VHX-600 is displayed in Figure 18.

Figure 18. The figure displays the Keyence VHX-600 digital optical microscope.

The Keyence V-Z500 lens is displayed in Figure 19. It is capable of magnifications up to 5000. The camera attaches to the lens's upper end and transmits the image to the monitor via cables.

Figure 19. The figure displays the Keyence VH-Z500 lens attached to the lens holder.

CHAPTER IV

EFFECTS OF STRAIN ON PROPERTIES OF METALLIC THIN-FILMS

This chapter discusses results obtained through microscopy and electrical resistance measurements. Effects of strain on physical properties of the gold and palladium thin-films an aluminum foil are studied. The latter is used for comparison.

4.1. Dimensions of Thin-films

Figure 20 displays the flat sample, which involves a 100 nm coating of gold and palladium on the surface of PVDF. It has a silver appearance and is approximately 1.7 cm long by 0.45 cm wide.

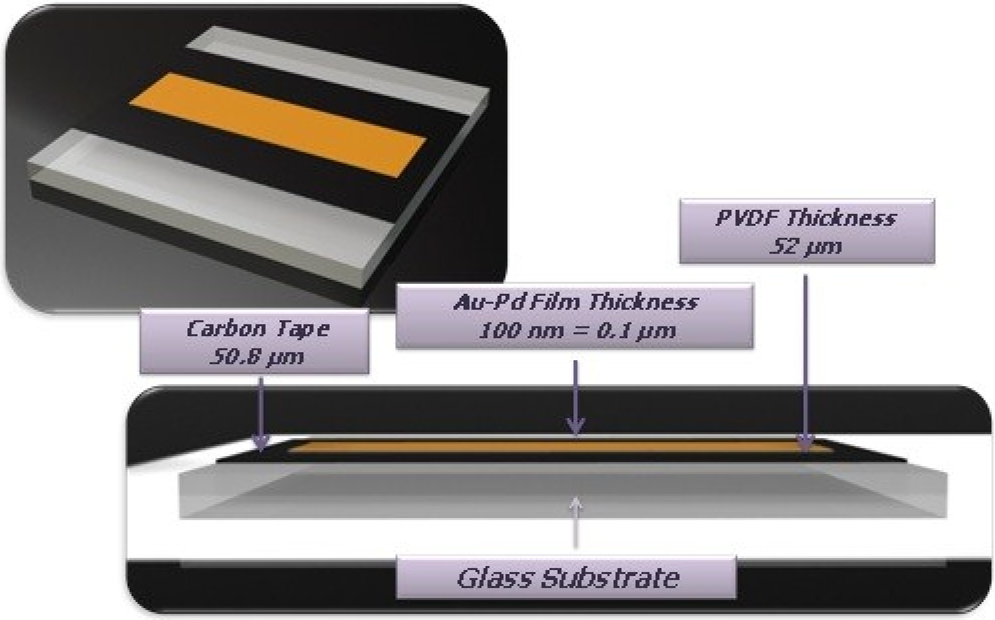

Figure 20. The figure displays the flat sample setup.

Figure 21 displays the convex sample. The induced normal strain, ε, for the convex sample is approximately $8.92 \times 10^{-6}\frac{m}{m}$ at the uppermost layer of the surface, and the calculation is provided in Equation 1:

$$\varepsilon = \frac{z}{\rho} = \frac{\frac{1}{2}t_{\text{Au-Pd}}}{R_{\text{cylinder}} + t_{\text{tape}} + t_{\text{PVDF}} + \frac{1}{2}t_{\text{Au-Pd}}} \qquad \text{Equation 1}$$

$$= \frac{\frac{1}{2}\left(100\times10^{-9}\text{m}\right)}{0.55\times10^{-2}\text{m}+50.8\times10^{-6}\text{m}+52\times10^{-6}\text{m}+\frac{1}{2}\left(100\times10^{-9}\text{m}\right)}$$

$$=8.92\times10^{-6}\frac{\text{m}}{\text{m}}$$

Here the z is the distance away from the neutral axis, ρ is the radius of curvature of the neutral axis, $t_{Au\text{-}Pd}$ is the thickness of the gold-palladium thin-film, $R_{cylinder}$ is the radius of the cylinder, t_{tape} is the thickness of the tape, and t_{PVDF} is the thickness of the PVDF. The neutral axis is the axis that contains no strain after deformation. The strain is tensile, and the calculation is based upon the Euler-Bernoulli beam theory [43]. Furthermore, the tensile strain decreases as one considers layers deeper into the surface of the material until one reaches the neutral axis. At the neutral axis, which exists 50 nm below the surface of the film according to the Euler-Bernoulli beam theory, there is no strain because there is no alteration in layer length. There is tensile strain above the neutral axis and compressive strain below the neutral axis. Because XPS only provides relevant data for approximately the top 5 nm of the material, the XPS shift that will be mentioned in the next chapter for a convex shape will entirely correspond to tensile strain [40].

Researchers have utilized the Euler-Bernoulli beam equation to calculate strain in lead zirconate titanate oxide (PZT) thin-films [44].

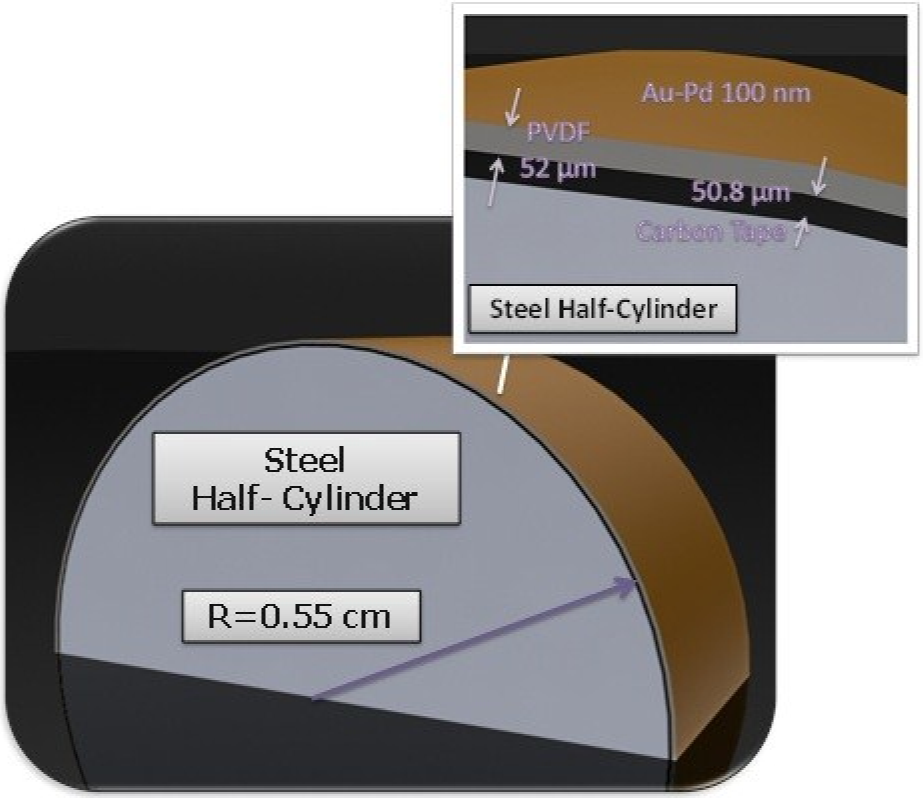

Figure 21. The figure displays the convex sample setup.

The strain in the convex shape is provided in Figure 22. The Euler-Bernoulli beam theory suggests that the strain varies linearly through the depth of the beam. The assumptions inherent to the Euler-Bernoulli beam theory include that sections that are plane stay plane after bending as well as no changes in thickness due to bending [45]. The region in which XPS data is measured is displayed in the red region in the figure.

Finally, the depth of the neutral axis is displayed, and it is demonstrated that tensile strain exists above the neutral axis whereas compressive strain exists below the neutral axis.

The convex shape experienced the greatest and most consistent shift in electron binding energy in comparison to the flat sample's electron binding energy. This shift occurs due to the applied strain as seen in the red region in Figure 22 in which the tensile strain varies between $8.03 \times 10^{-6}\ \frac{m}{m}$ and $8.92 \times 10^{-6}\ \frac{m}{m}$. Furthermore, there is a shift in the electrical conductivity of aluminum foil substrates when the substrate is bent into a convex shape. Finally, the convex shape experiences less energy loss due to plastic deformation than a flat sample.

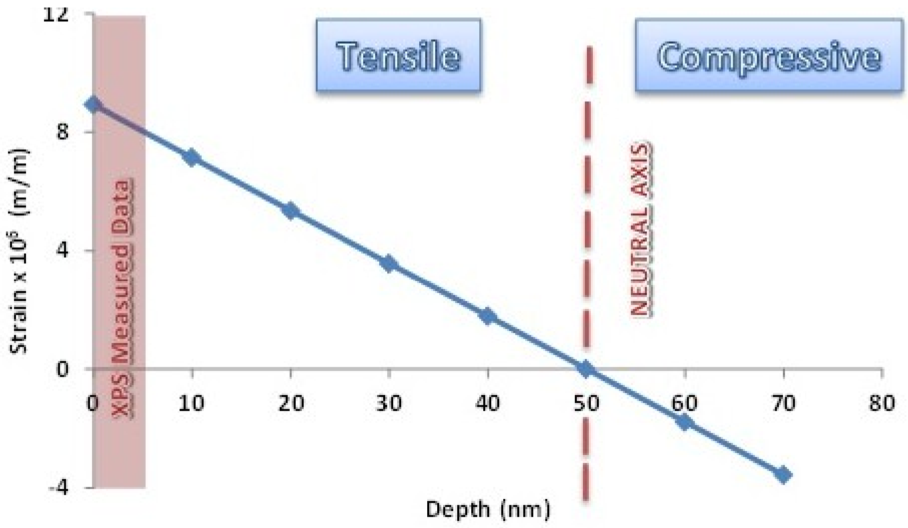

Figure 22. The figure displays the strain estimated by the Euler-Bernoulli beam theory in the convex sample as a function of depth.

Figure 23 displays the convex sample. The applied normal strain, ε, for the convex sample at the uppermost layer of the surface is approximately $-1.28 \times 10^{-5} \frac{m}{m}$ and the calculation is provided below. The calculation is based upon the Euler-Bernoulli beam theory and is provided in Equation 2. The strain is negative due to a compressive strain.

$$\varepsilon=-\frac{z}{\rho}=-\frac{\frac{1}{2}t_{\text{Au-Pd}}}{R_{\text{cylinder}}-t_{\text{tape}}-t_{\text{PVDF}}-\frac{1}{2}t_{\text{Au-Pd}}} \qquad \text{Equation 2}$$

$$=-\frac{\frac{1}{2}\left(100\times10^{-9}\text{m}\right)}{0.55\times10^{-2}\text{m}-50.8\times10^{-6}\text{m}-52\times10^{-6}\text{m}-\frac{1}{2}\left(100\times10^{-9}\text{m}\right)}$$

$$=-1.28\times10^{-5}\,\frac{\text{m}}{\text{m}}$$

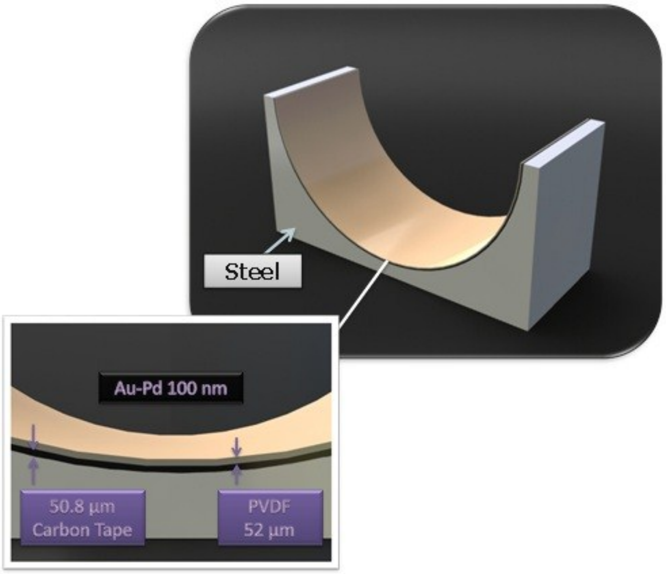

Figure 23. The figure displays the concave sample setup.

As will be discussed later, the aluminum foil in the concave arrangement experienced the greatest electrical resistance. It is necessary to comprehend the implications of the change in resistance of the substrate. It is likely that the changes in electron binding energy measured in this report and presented in the next chapter will lead to new sensing and actuation devices. Furthermore, this adjustment in the electrical resistance may be due to an alteration in the vacancy concentration of the material upon application of the strain.

4.2. Surface Morphology

Images of the gold and palladium surface are also provided via a digital optical microscope. It is interesting to view the surfaces from the digital optical microscope because it provides greater clarity for the researcher seeking to understand the surface of the PVDF before gold and palladium deposition. Furthermore, it allows the researcher to understand the sputter coating deposition process and how the gold and palladium adhere to the surface of the PVDF. The digital optical microscope used in this research provides high resolution images in both two dimensions and three dimensions. It allows the user to draw images on the screen. For instance, a circle may be drawn around a region of interest on the surface image of a material, and the instrument will provide an estimation to the diameter of the circle. Straight lines of known length may be drawn on the surface image of a material in order to estimate the sizes of various structures that appear on the surface. This is especially useful when examining materials of multiple phases. The digital optical microscope provides insight into surfaces of materials, and images from a digital optical microscope are provided in this chapter in order to make inferences about the surfaces of the PVDF and gold-palladium thin-films.

4.2.1. PVDF Substrate

PVDF, a ferroelectric polymer, is commonly used in medical imaging applications including thyroid imaging and ultrasound technologies due to its low acoustic impedance [46]. Furthermore, PVDF is commonly used in sensing technologies. For instance, PVDF has been implemented in the development of volume displacement sensors in order to control sound radiation [47]. In addition, tactile PVDF sensors have shown the ability to resolve shear stress components [48]. As will be discussed later, the shift in electron binding energy presented in this report provides a foundation for new sensing technologies, especially sensing techniques appropriate for nanomachines. Therefore, it is appropriate to choose a substrate for this new sensing technique that has already demonstrated success in sensor applications. Furthermore, before coating the PVDF substrate with the gold-palladium thin-films, it was appropriate to take images of the PVDF substrate with the digital optical microscope in order to view the PVDF before the coating process. An image of the PVDF substrate before gold and palladium deposition is displayed in Figure 24. The image was produced from a digital optical microscope with a magnification of 500. The PVDF is 52 micrometers in thickness and is transparent. It is distributed in large sheet form. Before the gold-palladium coating process, it was cut into small rectangular pieces that were approximately 1.7 cm long and 0.45 cm wide.

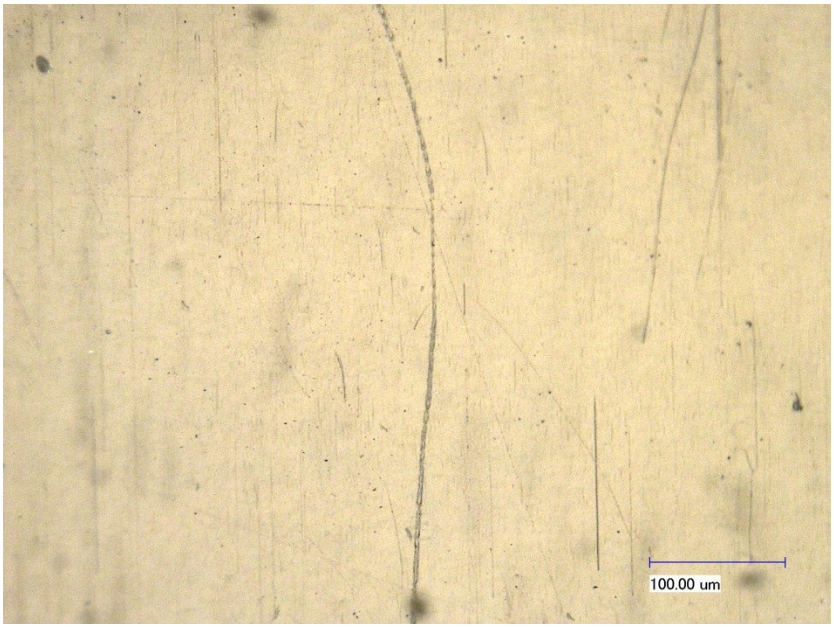

Figure 24. The PVDF is displayed at a magnification of 500 using a digital optical microscope.

An image of the PVDF substrate before gold and palladium deposition is displayed in Figure 25. The image was produced from a digital optical microscope with a magnification of 1000. It is evident that defects exist at the surface of the PVDF; however, it is anticipated that defects exist in the material. Thermodynamically, it is impossible to develop a material without defects. Additionally, it is shown in this report via digital optical microscope images that the gold and palladium adhered to the surface of the PVDF. Furthermore, XPS confirms the presence of gold and palladium to the surface of the PVDF.

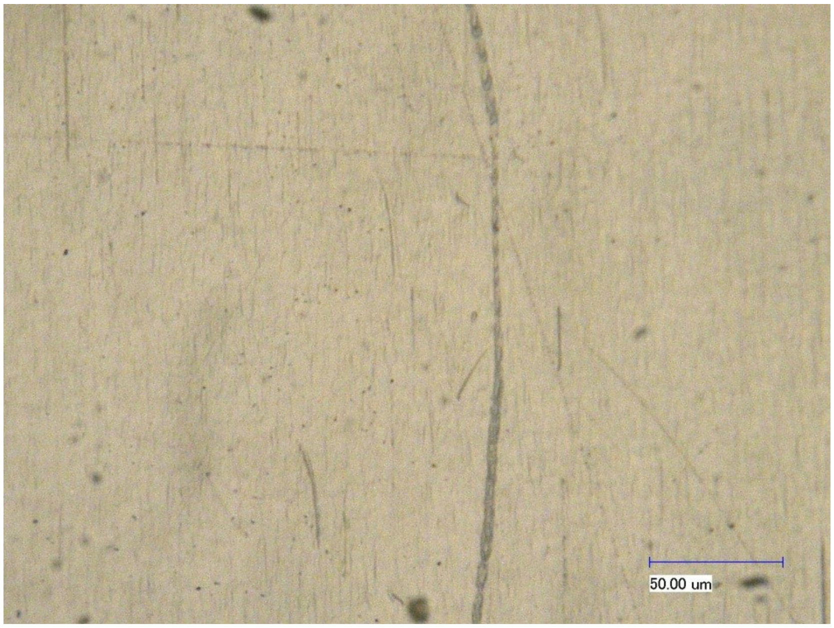

Figure 25. The PVDF is displayed at a magnification of 1000 using a digital optical microscope.

An image of the PVDF substrate before gold and palladium deposition is displayed in Figure 26. The image was produced from a digital optical microscope with a magnification of 2000. The surface morphology is displayed, and a long track is seen with dark circles in the image. These are likely defects, and the PVDF arrived from the manufacturer in this state. As previously stated, defects have little effect on the results from this report.

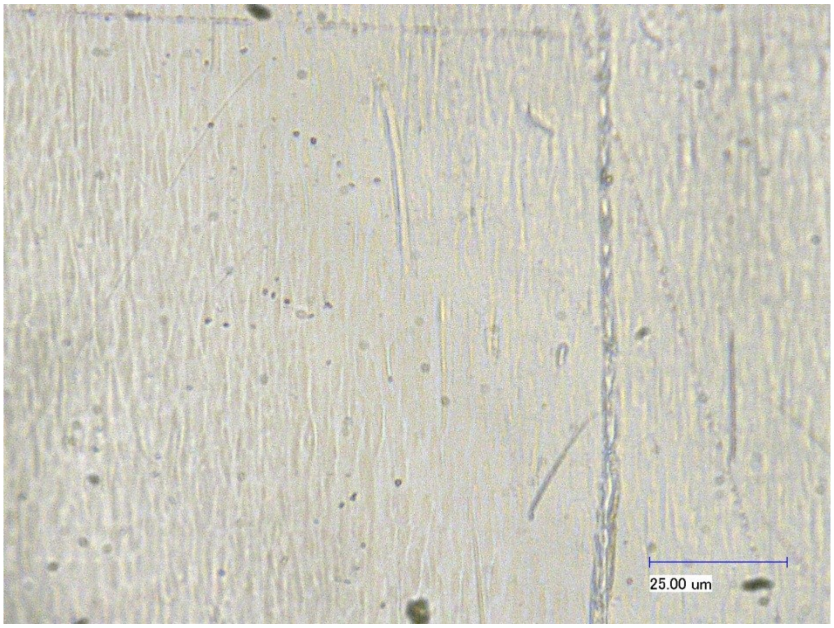

Figure 26. The PVDF is displayed at a magnification of 2000 using a digital optical microscope.

4.2.2. Gold and Palladium Sputtered on PVDF

PVDF was sputtered with a gold and palladium coating. The subsequent images display the gold and palladium microstructure using multiple magnifications. Furthermore, Figure 27 provides a three dimensional image using the digital optical microscope of the gold and palladium sputtered on the PVDF.

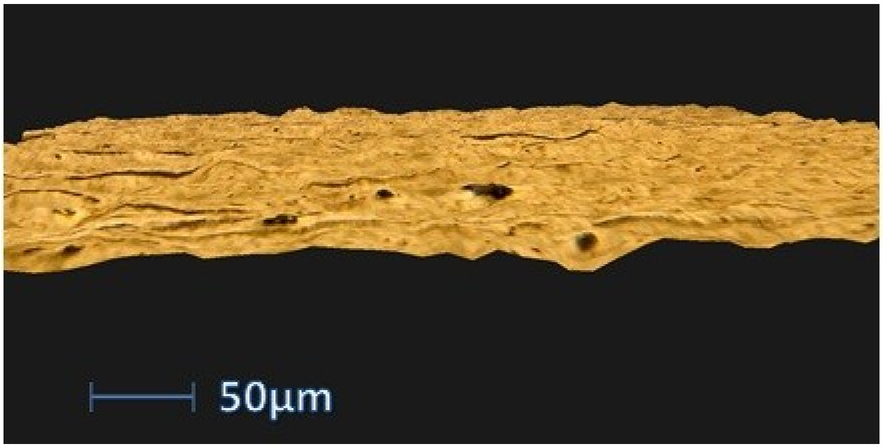

Figure 27. The gold and palladium were sputtered on PVDF and the resulting microstructure is displayed as a three dimensional image using the digital optical microscope.

This three-dimensional image is important for many reasons. First, it gives the researcher as well as the readers of this report a high magnification view of the gold and palladium sputtered on the PVDF surface in three dimensions. Next, it gives insight into the surface roughness. Finally, it facilitates for the researcher an iterative process for sputter coat deposition. Upon sputtering the surface of the PVDF with gold and palladium, the researcher can view a the sample in three dimensions. If the surface morphology does not align with the researcher's goal, then new films can be made and imaged with the digital optical microscope.

Figure 28 provides an image of the gold and palladium on a PVDF substrate in a flat arrangement with 500 magnification.

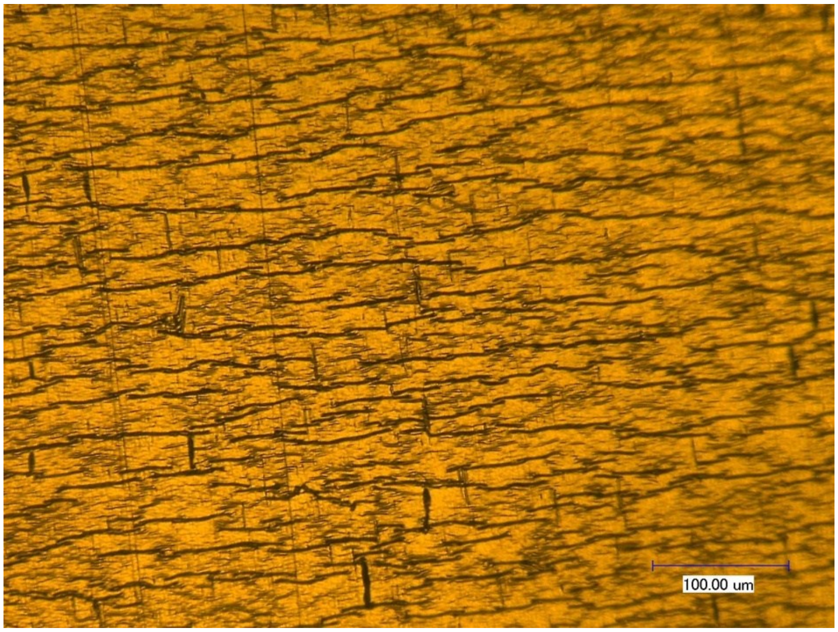

Figure 28. The Au-Pd film is displayed at 500 magnification deposited on a PVDF film.

Figure 29 provides an image of the gold and palladium on the PVDF substrate in a flat arrangement with 1000 magnification. The black lines indicate separation between the palladium and gold sputtered on PVDF. The sputter coat deposition process does not perfectly create a uniform thin-film. The film may be best described as a collection of gold and palladium islands connected together on the surface of PVDF.

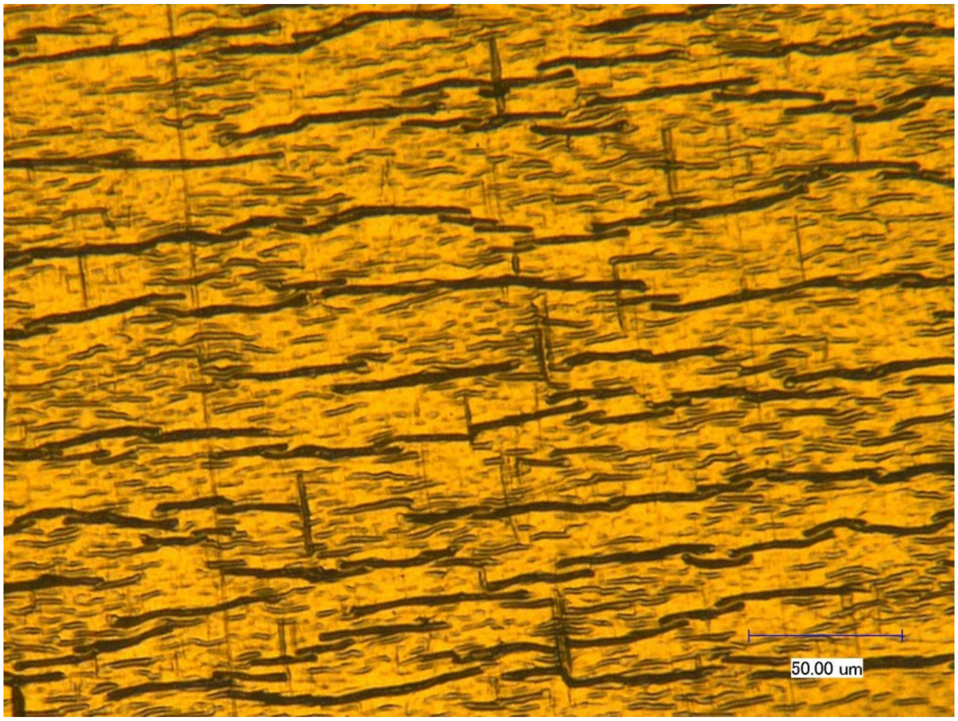

Figure 29. The Au-Pd film is displayed at 1000X magnification deposited on a PVDF film.

Figure 30 provides an image of the gold and palladium on the PVDF substrate in a flat arrangement with 2000 magnification.

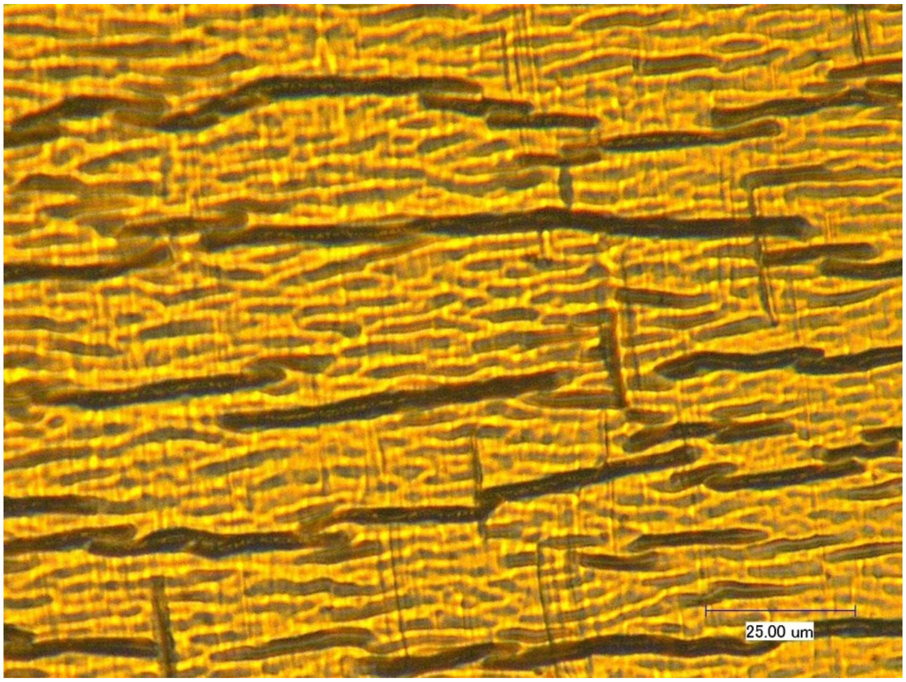

Figure 30. The Au-Pd film is displayed at 2000X magnification deposited on a PVDF film before the films were removed from the glass substrate.

Figure 31 provides an image of the gold and palladium on the PVDF substrate in a flat arrangement with 3000 magnification.

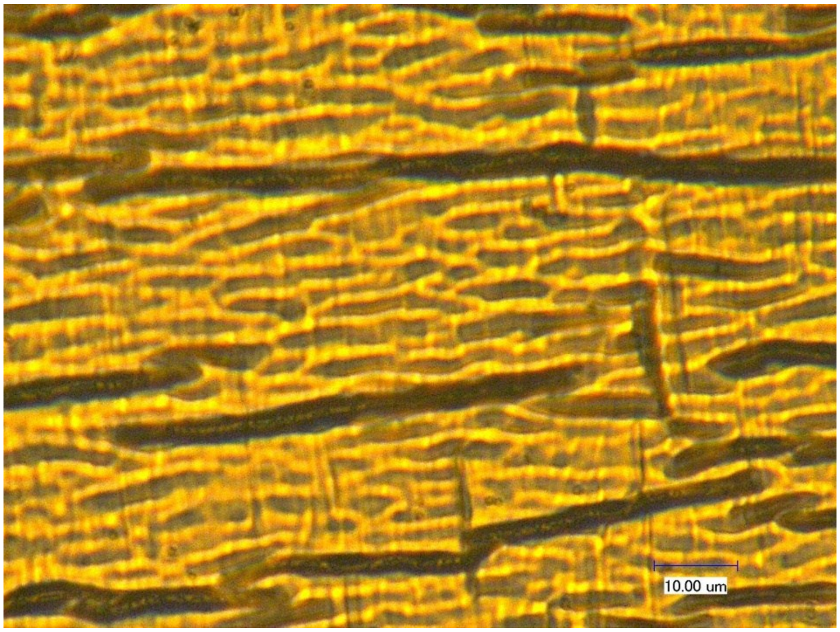

Figure 31. The Au-Pd film is displayed at 3000X magnification deposited on a PVDF film before the films were removed from the glass substrate.

Figure 32 provides an image of the gold and palladium on the PVDF substrate in a flat arrangement with 5000 magnification. The large magnification provides great insight into the surface morphology. It appears that the dark lines are separated by much smaller lines.

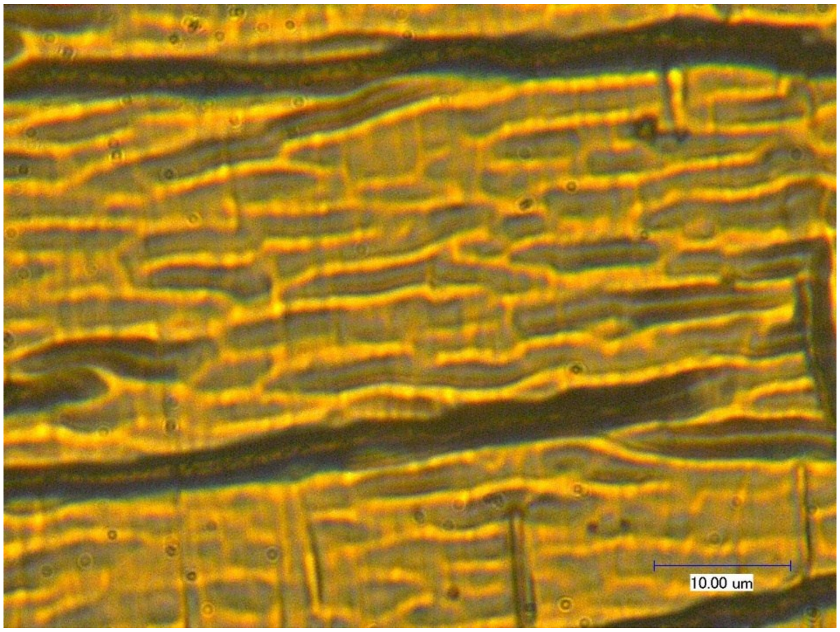

Figure 32. The Au-Pd film is displayed at 5000X magnification deposited on a PVDF film .

The appearance of islands or flakes of gold and palladium genuinely question the validity of the Euler-Bernoulli beam theory in its application to these films. However, these flakes or islands are interconnected and evenly dispersed across the surface of the PVDF. Furthermore, even if the Euler-Bernoulli beam theory cannot be perfectly applied to this situation, it can still give insight and an estimation into the strain in the top 5 nm of the material, where XPS data is extracted. Finally, it is appropriate to cite the Euler-Bernoulli beam theory as a method to estimate the strain in the top 5 nm in case future research into the XPS shift in electron binding energy featured in the next chapter is implemented with a gold and palladium coating that is much smoother. In such a case, the Euler-Bernoulli beam theory may more accurately describe the strain in the gold and palladium film.

Schematics of the samples produced for the experiments presented in this paper in Figs. 20-21 and 23 were displayed with calculations of the induced strain caused by stretching flat films over convex and concave shapes. As shown in Equations 1-2, the strain calculation was based from the Euler-Bernoulli beam theory. It was concluded that the strain at the uppermost surface of the convex shape was tensile and approximately $8.92 \times 10^{-6}\ \frac{m}{m}$, while the concave shape experienced a compressive strain on the surface with a magnitude of approximately $1.28 \times 10^{-5}\ \frac{m}{m}$. The magnitude of the strain is relevant because it provides the ability to correlate a strain with a change in energy loss via plastic deformation as well as a change in electron binding energy.

The surface morphology of the uncoated PVDF film substrate has been displayed using digital optical microscope images, as shown in Figs. 24-26. It was concluded that there are surface defects on the PVDF from the manufacturer; however, these defects do not prohibit the deposition of the gold and palladium on the PVDF surface. Next, images of the gold and palladium sputtered on the PVDF were also provided in Figs. 27-32. One of these images was a three-dimensional image of the PVDF with the gold and palladium coating that provided the readers another perspective of the thin-film system. It provided the researchers with an iterative technique to develop thin-films. In other words, the researchers could develop the thin-films, view a three dimensional image with the digital optical microscope, and subsequently produce more samples if the samples were not processed correctly.

The images produced from the digital optical microscope that the composition of the thin-films produced are less uniform in composition than desired due to the choice of sputter coat deposition. Sputtering has the advantage that it is a relatively quick method to produce samples, so many samples may be produced for testing purposes. However, the disadvantage that it provides concerns the uniformity of deposition. Other techniques, like evaporation deposition, provide a more uniform surface composition.

Thin-films' properties are different than bulk gold and bulk palladium properties because the thin-films have a dimension on the nanometer-scale, so surface characteristics become extremely important when determining mechanical properties. It has been demonstrated in previous research that the Young's modulus of gold thin-films is 53-55 GPa [49], while the Young's modulus of palladium thin-films with a thickness of approximately 110 nm is 233 GPa [50]. Therefore, it is expected that if either the gold-palladium thin-films forms a bimetallic alloy or if it forms a two phase system, then the Young's modulus of the film should be valued between these two extremes.

4.3. Electrical Resistance of Al Foil

In order to investigate how the applied strain via the change in shape affects the substrate electrical resistance, the resistance of an aluminum foil substrate was measured in flat, convex, and concave arrangements. The circuit to determine this value is provided in Figure 33. The resistance of the concave aluminum foil substrate was the largest, followed by the resistance of the convex surface and subsequently the resistance of the flat surface. A current-limiting resistor, R, was placed in the circuit in series with an aluminum foil substrate as well as an ammeter. The internal resistance of the circuit is considered to be the summation of the resistances of the aluminum foil substrate and the ammeter. Because the ammeter internal resistance remains approximately constant for each trial, the comparison of the internal resistance of the circuit provides a decent method to compare the changes in resistance between flat, convex, and concave aluminum foil substrates.

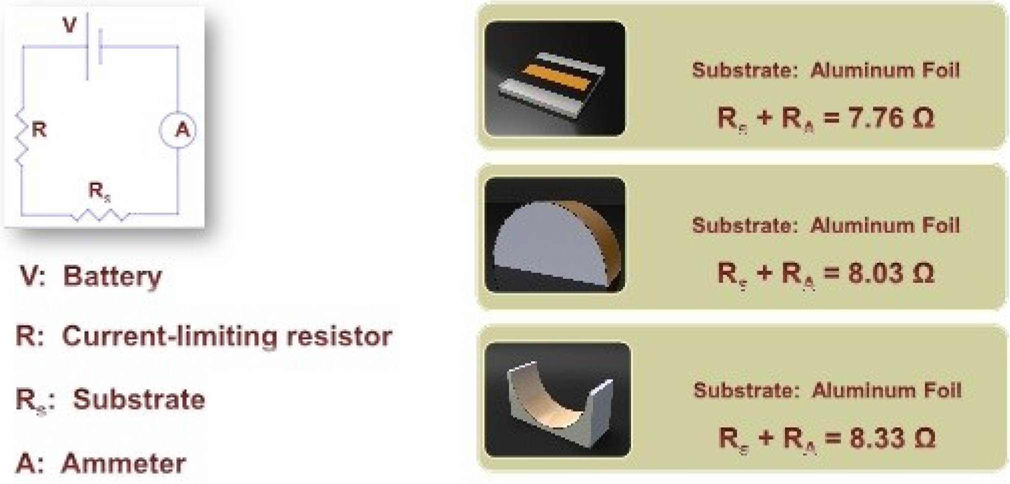

$$Internal\ Resistance = R_s + R_A = \frac{V}{I} - R$$

Figure 33. The figure displays the circuit and results of the aluminum foil substrate resistance measurement.

The results show that the concave shape experiences the greatest electrical resistance, followed by the convex and flat shapes, respectively. It is known that flat, convex, and concave shapes experience different vacancy concentrations in the lattice of the material [1]. Therefore, it is likely that this change in vacancy concentration leads to a change in electrical resistance. This is easily realized by envisioning the flow of electrons through the lattice. The electrons interact with the lattice, exchanging energy. A change in the vacancy concentration changes this interaction. A side effect of this interaction between the electrons and the lattice is heat; a wire that conducts electricity is often hot and may lead to burns if touched.

As shown in Figure 33, the concave shape experienced the greatest resistance, followed by the convex and flat shapes, respectively. It is necessary to understand the fluctuation of substrate resistance with change in shape due to the assertion that the XPS shift in electron binding energy displayed in the following chapter will likely be implemented in sensor technologies. Because sensors are implemented with circuits, it is obligatory to understand how a sensor's resistance is affected by strain, especially when that sensor's purpose is to convert strain into an electrical signal.

4.4. Nanomechanical Properties

Next, it was necessary to indent the samples using a nanoindenter. The nanoindenter indents the material to much smaller depths than a typical Vickers Hardness or Brinell Hardness test. There are numerous quantities that may be measured from an indentation experiment. For instance, a classical load-displacement plot is presented in Figure 34. In the figure, the slope of the unloading curve, $\frac{dP}{dh}$, is displayed with the plastic depth of penetration, h_p. The slope of the unloading curve may be utilized to estimate the effective modulus of the thin-films system, E_{eff}, via the equation $\boldsymbol{E_{eff}} = \frac{\mathbf{1}}{\mathbf{2}\boldsymbol{\beta}}\frac{\boldsymbol{dP}}{\boldsymbol{dh}}\sqrt{\frac{\pi}{A}}$ [51]. In this equation, β is a tip shape factor, which is 1.034 for the

Berkovich tip used in this research, and *A* is the area of indentation, which is $A = 3\sqrt{3}h_p^2 tan^2\theta$. For the Berkovich tip, $\theta = 65.27°$ and is the tip semi-angle. Furthermore, it is possible to extract the Young's modulus of the gold-palladium thin-films from the thin-films system through the equation $\frac{1}{E_{eff}} = \frac{(1-v_f^2)}{E_f}\left(1 - e^{-\frac{\alpha t}{\sqrt{A}}}\right) + \frac{(1-v_s^2)}{E_s}\left(e^{-\frac{\alpha t}{\sqrt{A}}}\right) + \frac{(1-v_i^2)}{E_i}$ [51]. In this equation, *f*, *i*, and *s* refer to film, indenter, and substrate, respectively. The values, *v*, *t*, and *α* in this equation refer to Poisson's ratio, the film thickness, and an empirical constant, respectively.

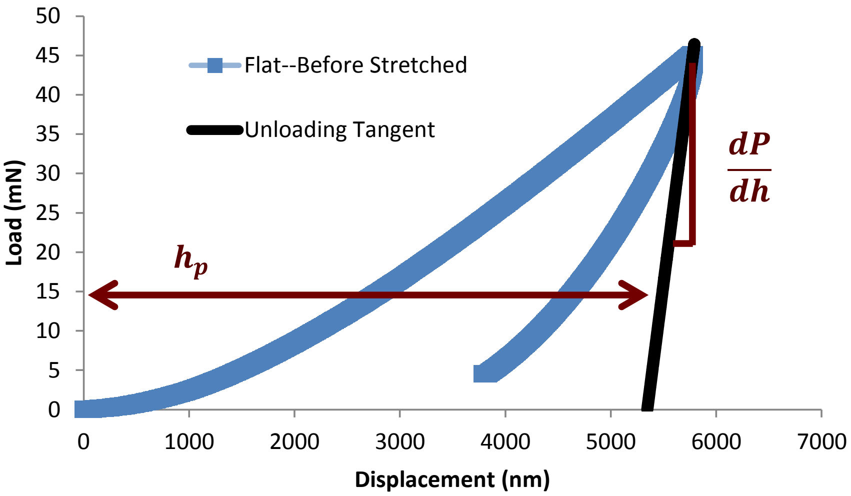

Figure 34. The figure displays a typical nanoindentation load-displacement plot.

The area underneath the load-displacement plot is the energy loss due to plastic deformation [51]. In order to estimate the area underneath the load-displacement curves, it was necessary to fit polynomials to the curves. Second-order polynomials were fit to the loading and unloading curves for the flat and convex samples. Next, integration was performed to determine the areas using MATLAB, and the program is provided.

```
% Flat
Greatest_Displacement = 1034.031707;
Final_Displacement = 590.8686919;
x = linspace(0,Greatest_Displacement,1e4);
f1 = 1.99e-6*x.^2+8.06e-4*x-3.28e-2;
f2 = (8.56e-6*x.^2-8.31e-3*x+2.26).*heaviside(x-Final_Displacement);
g = f1-f2;
Area_flat = trapz(x,g)*10^-12
Area_flat =
5.5475e-010
% Convex
Greatest_Displacement = 1106.000057;
Final_Displacement = 563.3623391;
x = linspace(0,Greatest_Displacement,1e4);
f1 = 1.80e-6*x.^2+6.82e-4*x-1.75e-2;
f2 = (4.40e-6*x.^2-2.69e-3*x+4.2e-1).*heaviside(x-Final_Displacement);
g = f1-f2;
```

```
Area_convex = trapz(x,g)*10^-12

Area_convex =

4.7798e-010
```

Furthermore, this change in in energy loss due to plastic deformation is provided in Figure 35. As can be seen, the convex shape lost less energy due to the plastic deformation than the flat shape. As will be indicated in the next chapter, this drop in energy lost via plastic deformation is accompanied by an increase in electron binding energy. It is proposed in this research that the stretching of the bonds causes the electrons to be attracted closer to the nuclei, and this is accompanied by a resistance to the flow of dislocations.

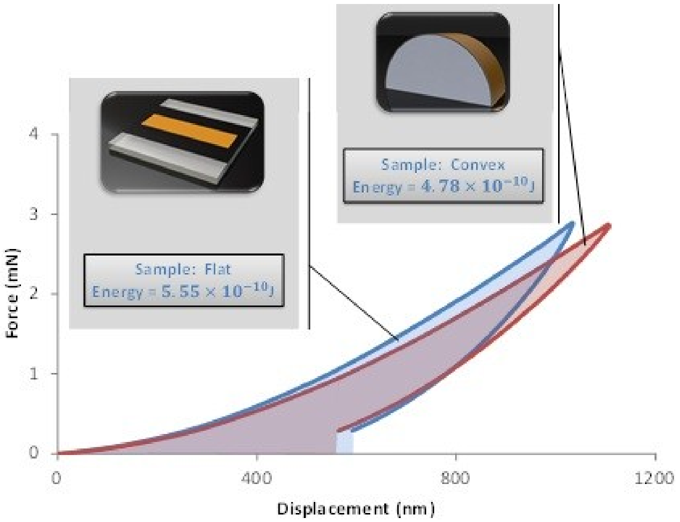

Figure 35. The figure displays the comparison between the indentations of flat and convex samples. There is less energy under the load-displacement plot of the convex sample than the flat sample.

As indicated in the nanoindentation, it exhibited a smaller area underneath the convex samples' load-displacement curve as opposed to the flat sample. In order to accurately compare a flat sample's energy loss via plastic deformation to the associated convex sample, it was a must to compare two tests with the same loading conditions. Results are shown in Figure 35 where the energy released as heat was $5.55 \times 10^{-5} J$ for the flat sample and was $4.78 \times 10^{-10}\text{J}$ for the convex sample This indicates that the convex sample experienced smaller energy loss due to plastic deformation than the flat sample, and it is known that plastic deformation exists because the unloading curve does not follow the loading curve upon the release of the load. This is attributed to the applied stretch in the convex sample. Because the bonds above the neutral axis of gold-palladium thin-film undergo a tensile stress, it is expected that it would need more activation energy to initiate plastic deformation [52]. Another possible explanation is the hardening. As known that metals become harder under stain due to interactions of dislocations. As a result, it requires more energy to further deform a metal after deformation. In the present work, the thickness of the thin-film is Approximately 100 nm. As in bulk materials, it is expected for the thin-films to have dislocation formation. The stresses required to move the dislocations in thin-films are often much greater than in the corresponding bulk material due to geometrical constraints [53]. Furthermore, strain fields surround dislocations. The strain applied by the stretch of the thin-film inhibits dislocation motion, causing the energy loss via plastic deformation to decrease.

This chapter discussed the surface morphology of the PVDF substrates and gold-palladium thin-films. The morphology discussions were enhanced by the digital optical microscope images in two and three dimensions It was determined that cracks exist on PVDF surface from the manufacturer, and slight cracks exist on the gold-palladium surface due to the sputter coating process. Furthermore, the effect of the applied strain on aluminum foil substrates is presented. It is determined that the concave shape exhibited the greatest resistance, followed by the convex and flat shapes, respectively. It was concluded that the application of the stretch induces a change in vacancy concentration, causing a change in electrical resistance. Finally, the stretch-induced change in the area beneath the load-displacement curve measured from indentation was presented. It was concluded that the area beneath the convex sample's load-displacement plot was smaller than the flat sample's load-displacement plot due to the increased activation energy as well as dislocation motion inhibition. The effects of strain on electronic binding energy will be discussed in next chapter.

CHAPTER V

EFFECTS OF STRAIN ON ELECTRON BINDING ENERGY OF THIN-FILMS

This chapter studies behavior of surface electrons of metallic thin-films. The effects of mechanical strain on binding energy of electrons will be discussed in the next chapter.

5.1. XPS

As discussed in Chapter I, the XPS was used to analyze thin-films of gold and palladium. The XPS detects the electrons located in a core-level position surrounds a nucleus. The amount of energy corresponds to the energy required to release a core-level electron from its orbit around the nucleus into the vacuum. Visible peaks exist in the spectrum at energies associated with the excitation of core-level electrons. Because each element maintains a unique XPS spectrum, the surface of a material may be distinctively identified.

5.2. Calibration

In Figure 36, the C (carbon) 1s peak for gold and palladium sputtered on a PVDF (polyvinylidene fluoride) substrate is displayed. It is always necessary to determine the binding energy associated with the C 1s peak for calibration purposes. Although there other peaks that are at times chosen for this calibration, the C 1s peak is often chosen because almost any material placed inside the chamber will have a detectable C 1s peak due to the fact that carbon is so common and its X-ray photoelectron spectroscopy peak is relatively invariant among samples. For the purposes of this experiment, the C 1s peak was always calibrated to 284.5 eV [54-65]. In other words, if the C 1s peak was measured to be 285.0 eV, then in order to effectively calibrate the measurements, 0.5 eV was subtracted from the full spectrum. In the case displayed in Figure 36, the C 1s peak was measured to be 281.9 eV, so 2.6 eV was added to the entire spectrum of electron binding energy measurements.

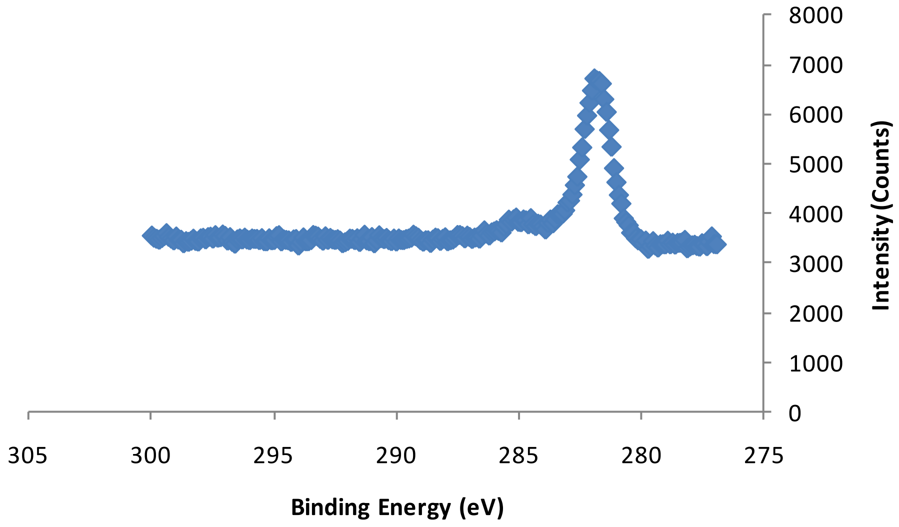

Figure 36. A C 1s peak is displayed as an example. The peak exists at 281.9 eV; therefore, in order to achieve a C 1s peak of 284.5 eV, all peaks' binding energies must be increased by 2.6 eV.

5.3. XPS of Gold and Palladium

In Figure 37, the gold X-ray photoelectron spectroscopy spectrum is displayed. The spectrum was shifted by 2.6 eV in order to account for the calibration procedure associated with the C 1s peak. The left peak is Au $4f_{5/2}$ and the right peak is Au $4f_{7/2}$.

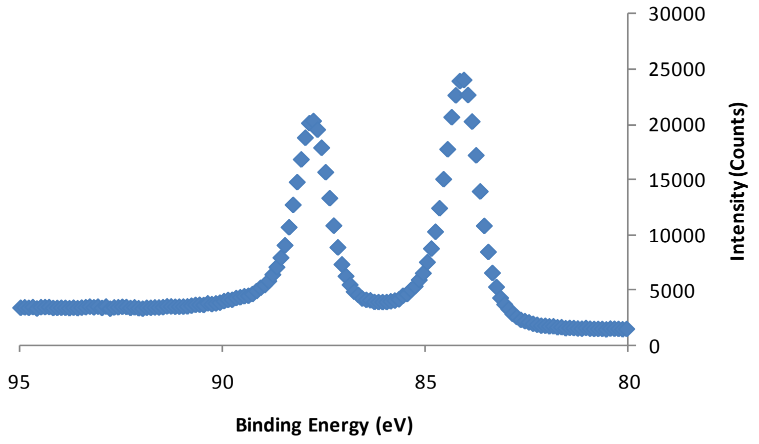

Figure 37. An example is displayed of a gold XPS spectrum. The raw data has been shifted by 2.6 eV as prescribed in Figure 36.

After obtaining the raw data, it is mandatory to fit the peaks in order to eliminate noise in the associated spectra. One physical explanation for such noise involves the escape of photoelectrons from relatively deep within the material. After excitation from the incident X-rays, some photoelectrons from deep within the material escape after colliding with the lattice. This causes the photoelectrons to escape from the sample material surface with less kinetic energy than had they escaped without colliding with the lattice. This decrease in kinetic energy displays in the XPS spectrum as false increase in potential energy. This leads to a background that, in general, increases with increasing binding energy. The curve fitting software attempts to estimate this background. The curve fitting software entitled *XPSPeak* was utilized. It is available for download online at http://www.uksaf.org/software.html.

In Figure 38, the results of curve fitting the raw data from Figure 37 are displayed. As seen in Figure 38, a blue line exists that corresponds to the estimated background that increases with increasing electron binding energy. Next, there is a red line that corresponds to the Au $4f_{7/2}$ peak as well as a green line that corresponds to the Au $4f_{5/2}$ peak.

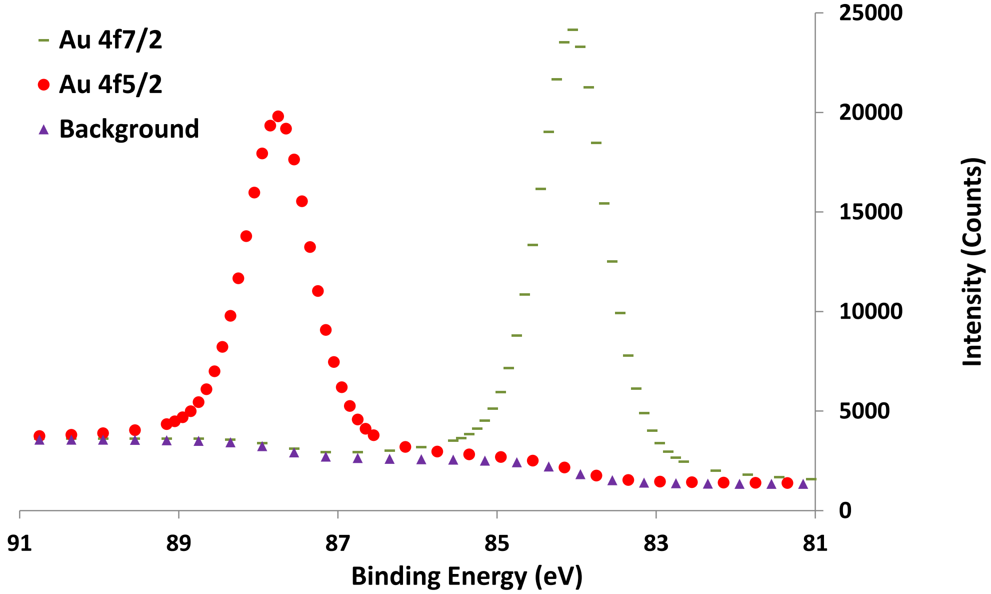

Figure 38. An example is displayed of a gold XPS spectrum after the application of a curve-fitting software.

The raw data for palladium peaks are presented in Figure 39. Upon inspection, there appears to be four peaks. The two primary peaks, Pd $3d_{3/2}$ and Pd $3d_{5/2}$ have been oxidized to produce two additional peaks. The oxidized peaks maintain slightly higher electron binding energy than the metallic peaks due to the notion that the core electrons in the palladium-oxygen bond are held tighter to the respective nuclei than the electrons from the palladium-palladium bond. A further explanation of this phenomenon is provided later in this chapter.

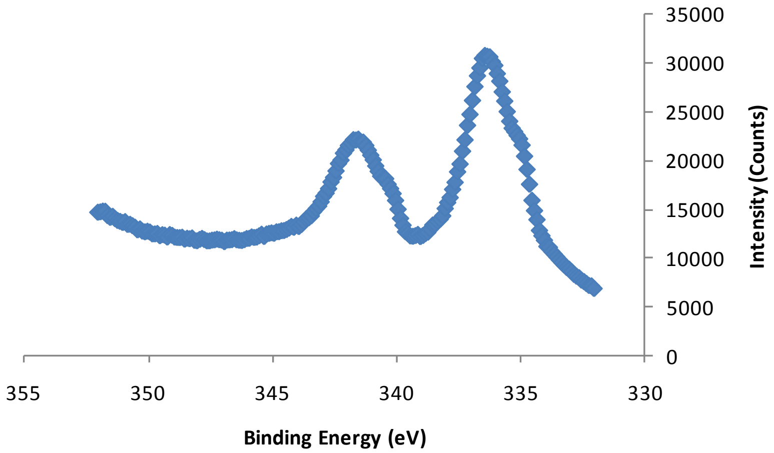

Figure 39. An example is displayed of a palladium XPS spectrum. The raw data has been shifted by 2.6 eV as prescribed in Figure 36.

Of course, similar to the curve fitting of the gold XPS spectrum, it is also necessary to fit curves to the palladium data using curve fitting software. The result is displayed in Figure 40. Five curves are displayed in the figure. First, it was necessary to provide a background curve. Next, there are two curves associated with the Pd $3d_{3/2}$ and Pd $3d_{5/2}$ binding energies due to electrons that escaped from palladium-palladium bonds. Finally, there are two curves associated with the Pd $3d_{3/2}$ and Pd $3d_{5/2}$ binding energies due to electrons that escaped from palladium-oxygen bonds.

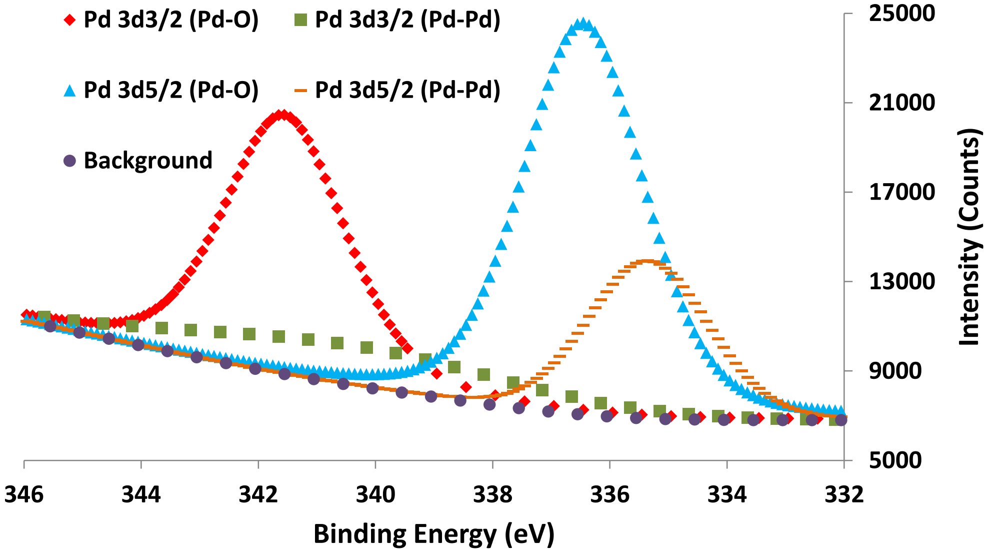

Figure 40. An example is displayed of a palladium XPS spectrum after the application of a curve-fitting software.

The previous graphs displayed the results of only one test. To properly characterize the elements' electron binding energies in the thin-films, it is necessary to perform multiple tests in order to minimize the uncertainty associated with the XPS results. Therefore, six tests of the gold and palladium sputtered PVDF samples were independently measured for both flat and convex shapes. Figure 41 provides the peaks determined from the curve fitting software based from an average of six trials for the gold XPS spectrum on flat PVDF substrates. Before the curve fitting procedure, the calibrated raw data was averaged. The peaks were located at 87.45 eV and 83.85 eV for peaks of $4f_{5/2}$ and $4f_{7/2}$, respectively.

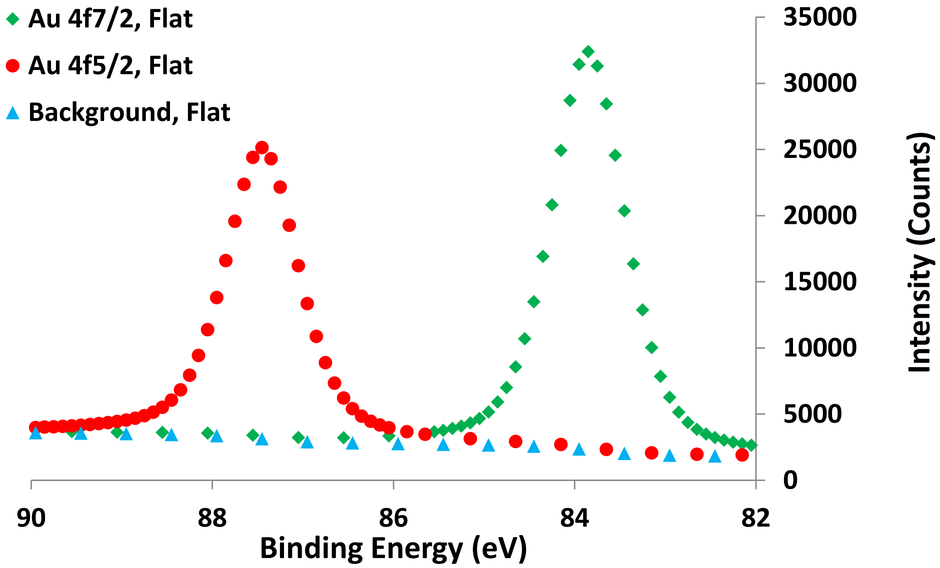

Figure 41. The figure displays the gold curve-fitted XPS spectrum from flat PVDF substrates with peaks occurring at 87.45 eV and 83.85 eV for the Au $4f_{5/2}$ and Au $4f_{7/2}$ peaks, respectively.

Likewise, Figure 42 displays gold curve-fitted XPS spectra on convex PVDF substrates, and the curve fitting was performed on the average of six calibrated raw data sets. The peaks were located at 87.75 eV and 84.05 eV for Au $4f_{5/2}$ and Au $4f_{7/2}$ peaks, respectively. It is useful to compare Figure 41 to Figure 42 in order to understand the difference between the electron binding energies associated with flat and convex shapes, and this comparison is provided in Figure 43 with the averaged raw calibrated data overlaid.

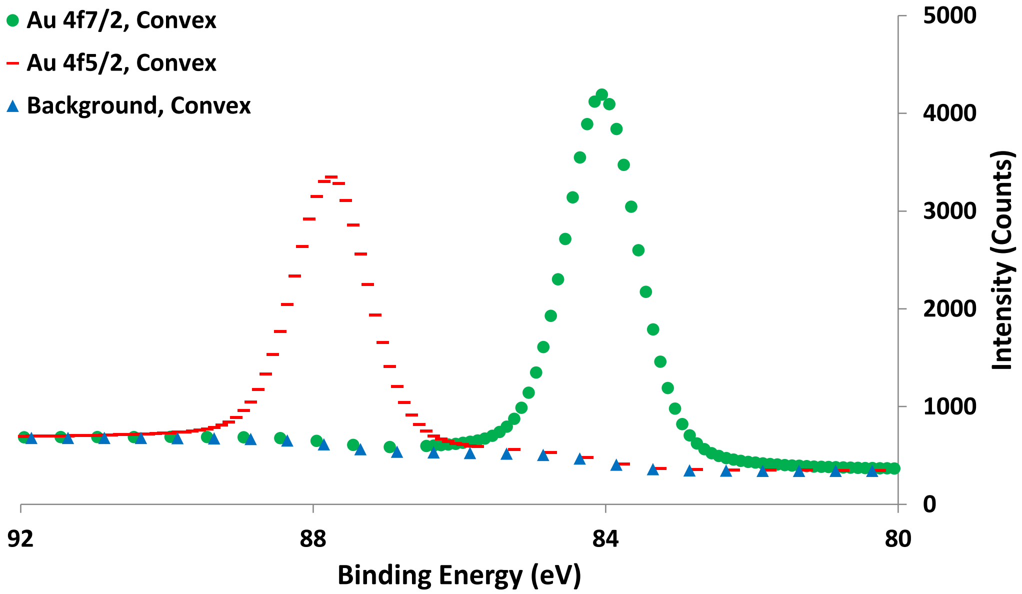

Figure 42. The figure displays the gold curve-fitted XPS spectrum from convex PVDF substrates with peaks occurring at 87.75 eV and 84.05 eV for the peaks of $4f_{5/2}$ and $4f_{7/2}$, respectively.

Figure 43 shows results from Figure 41 combined with the data from Figure 42 overlaid with the averaged calibrated raw data in order to compare the flat and convex samples. It is apparent that the convex samples maintain greater electron binding energies for gold than the corresponding flat samples. In fact, this shift in electron binding energy is quantifiable. For the Au $4f_{5/2}$ electronic state, the convex sample experienced a 0.3 eV increase in electron binding energy in comparison to the flat sample whereas when considering the Au $4f_{7/2}$ electronic state, the convex sample experienced a 0.2 eV increase in electron binding energy in comparison to the flat sample.

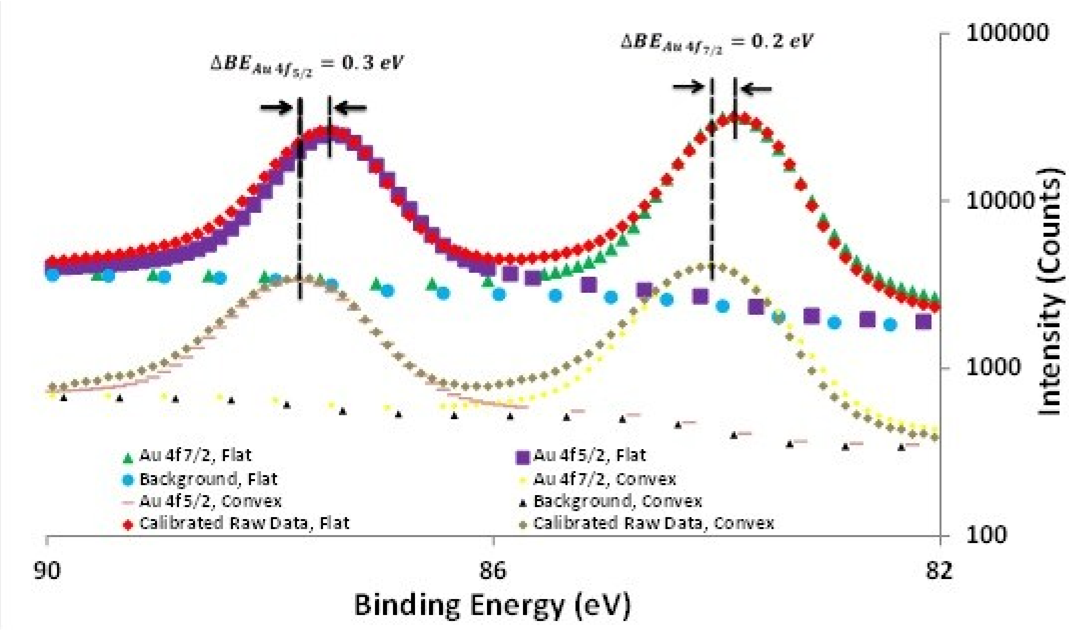

Figure 43. Gold curve-fitted XPS spectra for flat and convex samples are displayed in the figure with the averaged calibrated raw data. An increase in the electron binding energy is evident for the convex samples in comparison to the flat samples.

Figure 44 provides an average of six trials for palladium electron binding energy peaks for flat samples on PVDF substrates. In other words, the peaks within the palladium calibrated raw data physically represent the summation of multiple peaks. This can easily be seen in the calibrated raw data of Figure 44 where the spectrum exhibits asymmetric peaks, indicating peaks within peaks. The best explanation for the difference in peak behavior between the gold peaks and the palladium peaks lies in the bonding characteristics of the gold and palladium. Both gold and palladium have filled d-bands in the atomic state; however, when palladium atoms bond to other atoms, the d-band loses electron occupancy to the sp-band [65]. Therefore, palladium is not a noble metal like gold [65]. Furthermore, it has been shown that palladium acts as a catalyst for oxidation of CO by O_2 [66]. From this evidence, it is established that the additional peaks exhibited in the palladium spectrum are indicative of oxidized peaks. It is critical to be able to estimate the location of these peaks. Previous research has shown that the oxidized palladium peaks exhibit greater binding energy than the metallic palladium peaks in 10^{-1} and 10^{-3} millibar 0_2 ranges [67, 68]. Furthermore, literature suggests that the Pd $3d_{5/2}$ peak exists at 335.1 eV, while the oxide peaks exist in the ranges of 336-336.5 eV and 337.8-338.2 eV for PdO and PdO_2, respectively [69]. Regarding the flat samples in the present research, the peaks are located at 340.65 eV and 335.35 eV for $3d_{3/2}$ and $3d_{5/2}$, respectively, and these peaks are associated with electrons from palladium-oxygen bonds. Furthermore, the peaks associated with the palladium metallic bonds are located at 340.45 eV and 335.15 eV for $3d_{3/2}$ and $3d_{5/2}$, respectively.

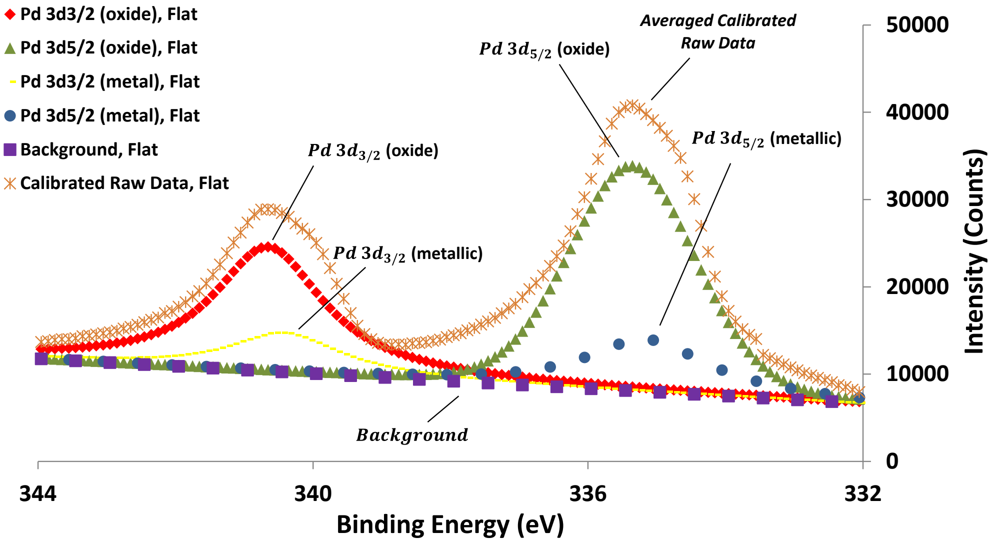

Figure 44. The average calibrated raw data of six tests for the palladium XPS spectrum measured from flat samples is displayed with the peaks generated from the XPS curve fitting software. The oxidized palladium peaks are located at 340.65 eV and 335.35 eV for Pd $3d_{3/2}$ and Pd $3d_{5/2}$, respectively. The metallic palladium peaks are located at 340.45 eV and 335.15 eV for Pd $3d_{3/2}$ and Pd $3d_{5/2}$, respectively.

Figure 45 provides an average of six trials for palladium electron binding energy peaks for convex samples on PVDF substrates. The peaks are located at 341.95 eV and 336.75 eV for Pd $3d_{3/2}$ and Pd $3d_{5/2}$, respectively, and these peaks are associated with the oxidized palladium peaks. Furthermore, the metallic palladium peaks are located at 340.85 eV and 335.55 eV for Pd $3d_{3/2}$ and Pd $3d_{5/2}$, respectively. The six sets of calibrated raw data were averaged, and the peaks were determined via the curve fitting software from the averaged calibrated raw data.

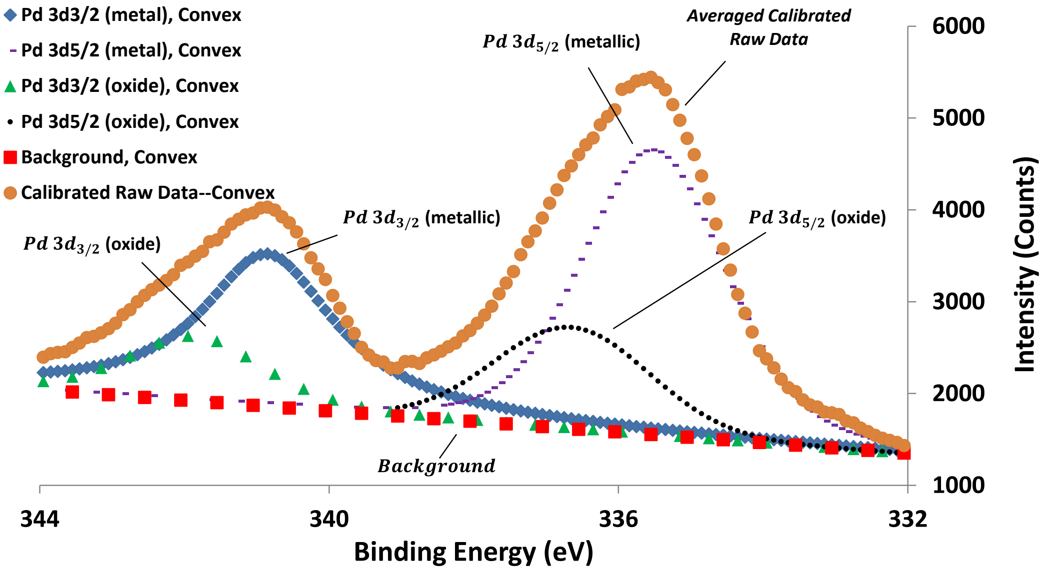

Figure 45. The average calibrated raw data of six tests for the palladium XPS spectrum measured from convex samples is displayed with the peaks generated from the XPS curve fitting software. The oxidized palladium peaks are located at 341.95 eV and 336.75 eV for Pd $3d_{3/2}$ and Pd $3d_{5/2}$, respectively. The metallic palladium peaks are located at 340.85 eV and 335.55 eV for Pd $3d_{3/2}$ and Pd $3d_{5/2}$, respectively.

Figure 46 provides the data from Figure 44 combined with the data from Figure 45 in order to provide for a comparison between the flat and convex substrates. It is apparent that the convex samples maintain greater electron binding energies for palladium than the corresponding flat samples. In fact, this shift in electron binding energy is quantifiable. For the Pd $3d_{3/2}$ electronic state, the convex sample experienced a 1.3 eV increase for the oxidized palladium peak and a 0.4 eV increase for the metallic palladium peak in comparison to the flat sample whereas when considering the Pd $3d_{5/2}$ electronic state, 1.4 eV increase for the oxidized palladium peak and a 0.4 eV increase for the metallic palladium peak in comparison to the flat sample.

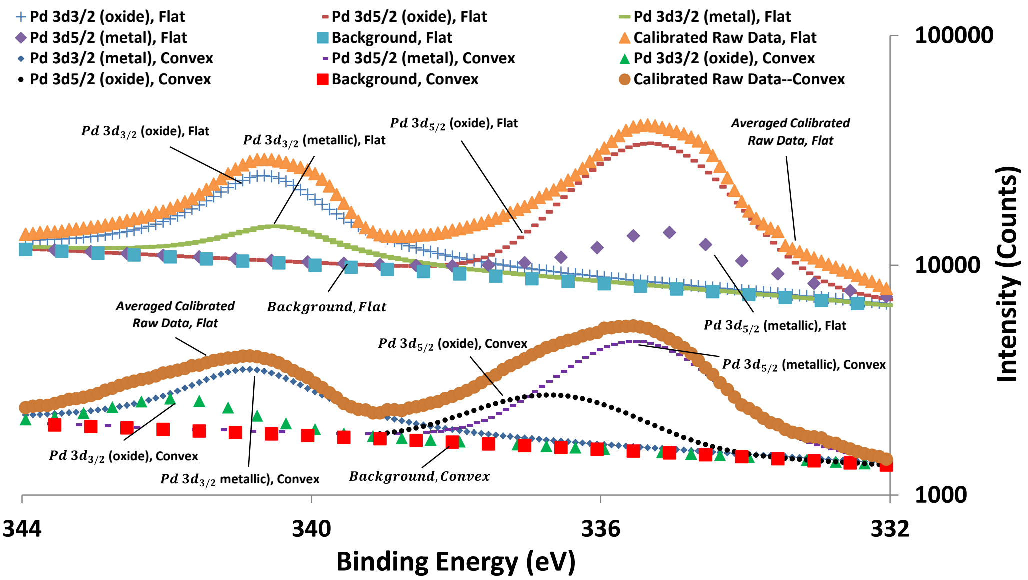

Figure 46. Palladium curve-fitted XPS spectra for flat and convex samples are displayed in the figure with the averaged calibrated raw data. An increase in the electron binding energy is evident for the convex sample in comparison to the flat sample.

The oxidized palladium peaks for the flat samples only maintain peaks at binding energies of 0.2 eV greater than the corresponding metallic palladium peaks. This is in comparison to the convex sample which maintains oxidized palladium peaks that are located at positions that are 1.1-1.2 eV greater than the corresponding metallic palladium peaks. From the literature [16], the 1.1-1.2 eV increase seems more reasonable and also suggests that the oxidation is more likely the formation of PdO as opposed to PdO_2. Furthermore, the relatively small increase of oxidized palladium peaks experienced by the flat samples may be explained by a few reasons. First, averaging the calibrated raw data may induce some bias in the final location of the oxidized palladium peaks. Second, the software determines the location of the oxidized peaks if they are not explicitly fixed by the user. It is possible for the researcher to fix the location of the oxidized palladium peaks in the software by using a reference; however, this may not capture the actual behavior of the tested samples. Instead, if the user does not explicitly state the location of the peaks, the software uses a statistical technique to determine the location by minimizing chi-square. In this research, the locations of the oxidized peaks were determined by minimizing chi-square. Third, it is possible that multiple oxidation peaks exist. The attempts to fit more than two oxidation peaks in the curve fitting software for flat and convex samples did not seem to accurately reflect the behavior of the system.

The greatest implication of this research is its capability to be used in unique sensing devices. For instance, it may be possible to estimate the strain at a particular point in a nanogear via known shifts in electron binding energy due to applied strain. This notion will be presented in greater detail in the subsequent chapter. Furthermore, the research suggests a direct relation between the increase in electron binding energy and decrease in energy loss via plastic deformation as measured by the load-displacement curve of indentation measurements. When the bonds are stretched over the convex surface, there is a transfer of energy via the stretched bonds. If examined in terms of the Lennard-Jones potential, there is an increase in the atomic binding energy upon increasing the distance between the atoms situated in the potential well. The implication is direct relationship between this increase in energy that has been directed to the lattice and the amount of energy lost. The area beneath the loading curve is indicative of the energy that the material absorbs from the indentation, whereas the area beneath the unloading curve represents the energy that the material releases upon release of the sample from the load. The difference, or the area between the loading and unloading plots, indicates energy lost via plastic deformation in the form of heat. It was demonstrated in the last chapter that there is less heat generated from the plastic deformation of the convex sample than the flat sample. This spectacle is related to the transfer of energy to the lattice from the applied strain, which in turn is related to the increase in electron binding energy.

.

CHAPTER VI
CONCLUSIONS AND FUTURE RECOMMENDATION

This research investigated the effects of mechanical strain on electronic binding energy of thin-films using XPS. A connection was established between the shift in electron binding energy and the area beneath the indentation load-displacement curve. It was demonstrated that the applied strain via the change in shape caused increases in the electron binding energy in gold and palladium by 0.2 eV to 1.4 eV and a decrease in the area beneath the indentation load-displacement curve from 5.55×10^{-10} J to 4.78×10^{-10} J. Furthermore, aluminum foil resistance was demonstrated to increase when stretched; the circuit's internal resistance increased by 0.27 Ω and 0.57 Ω for convex and concave shapes, respectively, when compared to flat aluminum foil.

If the shift in electron binding energy due to the applied stretch phenomenon is going to be used in sensing and actuation applications, it will be necessary to understand how resistance is affected by applied strain. Of course, sensors are implemented into circuits in order to convert a physical quantity into an electrical signal. If strain is converted into an electrical signal, it is necessary to appreciate how strain affects resistance. This report indicates that strain applied via a convex shape increases the resistance of the substrate material.

The future implications of the shift in electron binding energy due to the applied stretch in thin-films may be vast. The shift measured in this research may provide new sensing capabilities. As the discovery of the piezoelectric effect facilitated the advancement of new sensing and actuation technologies, it is determined that the shift in electron binding energy due to the applied stretch may also provide new avenues for sensing and actuation technologies. It is proposed that this research should be used in future sensing applications. For instance, nanoelectromechanical systems (NEMS) and microelectromechanical systems (MEMS) operate with the use of instruments at relatively small length scales. Of course, some of the associated parts may exhibit strain due to applied stresses from normal use. A nanogear may deform in a nanomachine due to high stresses. It will be necessary to analyze the applied strain, and this may be difficult analytically and numerically because computer models are often inaccurate, especially at such small length scales. Furthermore, it is almost always preferable for researchers to be able to test quantities as opposed to relying on calculations; therefore, it is proposed that this known shift in electron binding energy due to the applied stretch may be used in the case of estimating strain in parts at the micro and nano-length scales. It can be envisioned that if a researcher would like to estimate the strain in a nanogear, then the gear may be placed in an XPS instrument with the X-ray beam aimed at the strained area to measure the shift in electron binding energy. The shift may be determined by comparing the electron binding energy of the strained part to the electron binding energy of a part that has not been strained. On must be careful to ensure that the X-ray beam is aimed at the same location on each part.

REFERENCES

[1] M.W. Barsoum, Fundamentals of Ceramics, McGraw-Hill, New York (1997).

[2] P. Kumar, Elements Of Fracture Mechanics, Tata McGraw-Hill Education, New Delhi (2009).

[3] A.J. McEvily, Metal Failures: Mechanisms, Analysis, Prevention, John Wiley & Sons, Inc., New York (2002).

[4] J.A. Collins, Failure of Materials in Mechanical Design: Analysis, Prediction, Prevention, John Wiley & Sons, Inc., New York (1993).

[5] J.R. Davis, ASM Specialty Handbook: Stainless Steels, ASM International, Materials Park (1994).

[6] M.K. Beyer, H. Clausen-Schaumann, Chem. Rev. 105 (2005) 2921-2948.

[7] A. Katchalsky, M. Zwick, J. Polym. Sci. 16 (1955) 221-234.

[8] T. Tsuzuki, P.G. McCormick, J. Mat. Sci. 39 (2004) 5143-5146.

[9] V.V. Boldyrev, E.G. Avvakumov, Rus. Chem. Rev. 40 (1971) 847-859.

[10] J.J. Gilman, Science 274 (1996) 65.

[11] H. Pan, L. Liu, Z. Guo, L. Dai, F. Zhang, D. Zhu, R. Czerw, D.L. Carroll, Nano Lett. 3 (2003) 29-32.

[12] S. Karthikeyan, R.P. Sijbesma, Nature Chem. 2 (2010) 436-437.

[13] J. Xue, D. Wan, S. Lee, J. Wang, J. Am. Ceram. Soc. 82 (1999) 1687-1692.

[14] D. Keller, C. Bustamante, Biophys. J. 78 (2000) 541-556.

[15] M.F. Iozzi, T. Helgaker, E. Uggerud, Mol. Phys. 107 (2009) 2537-2546.

[16] E.M. Gutman, G. Solovioff, D. Eliezer, Corros. Sci. 38 (1996) 1141-1145.

[17] P.G. McCormick, F.H. Froes, JOM J. Min. Met. Mat. S. 50 (1998) 61-65.

[18] C. Suryanarayana, Prog. Mat. Sci. 46 (2001) 1-184.

[19] A.L. Companion, Chemical Bonding, McGraw-Hill, New York (1979).

[20] J.D. Renton, Applied Elasticity: Matrix and Tensor Analysis of Elastic Continua, Ellis Horwood, Chichester, UK (1987).

[21] J. Stewart, Calculus: Early Vectors, Brooks/Cole, Pacific Grove, CA (1999).

[22] N.C. Saha, H.G. Tompkins, J. Appl. Phys. 72 (1992) 3072-3079.

[23] J.R. Shallenberger, D.A. Cole, S.W. Novak, J. Vac. Sci. Technol., A 17 (1999) 1086-1090.

[24] H. Chandler, Hardness Testing, ASM International, Materials Park, OH (1999).

[25] V.E. Lysaght, Indentation Hardness Testing, Reinhold Pub. Corp., New York (1949).

[26] S.R. Williams, Hardness and Hardness Measurements, The American Society for Metals, Cleveland, OH (1942).

[27] P. Walker, W.H. Tarn, CRC Handbook of Metal Etchants, CRC Press, Boca Raton, FL (1991).

[28] C. Radloff, N.J. Halas, Appl. Phys. Lett. 79 (2001) 674-676.

[29] F. Edler, M. Kuhne, E. Tegeler, Metrologia 41 (2004) 47-55.

[30] O.L. Anderson, D.G. Isaak, S. Yamamoto, J. Appl. Phys. 65 (1989) 1534-1543.

[31] L.J. Gillespie, L.S. Galstaun, J. Am. Chem. Soc. 58 (1936) 2565-2573.

[32] J.W. Farah, R.G. Craig, D.L. Sikarskie, J. Biomech. 6 (1973) 511-514.

[33] S.G. Lin, J.H. Constable, W. Brodsky, G.H. Thiel, D.C. Sun, 47th Elect. Comp. Tech. Conf. Proc. (1997) 1105-1109.

[34] G. Rochat, Y. Leterrier, P. Fayet, J.A.E. Manson, Thin Solid Films 437 (2003) 204-210.

[35] R.W. Berry, P.M. Hall, M.T. Harris, Thin Film Technology, Van Nostrand, Princeton, NJ (1968).

[36] K.K. Schuegraf, Handbook of Thin-Film Deposition Processes and Techniques: Principles, Methods, Equipment, and Applications, Noyes Publications, Park Ridge, NJ (1988).

[37] J.L. Vossen, W. Kern, Thin film Processes II, Academic Press, Boston (1991).

[38] M. Pelliccione, T. Lu, Evolution of Thin-Film morphology: Modeling and Simulations, Springer, New York (2008).

[39] H. Pettersson, D. Allison, G. Schulthess, H. Smith, The Encyclopaedia of Medical Imaging, The NICER Institute, Oslo, Norway (1998).

[40] V.I. Nefedov, X-ray Photoelectron Spectroscopy of Solid Surfaces, VSP BV, Utrecht, Netherlands (1988).

[41] Kratos Analytical, AXIS HSi 165 and ULTRA Operators Manual, <http://www.kratos.com> (2009).

[42] D. Tranchida, S. Piccarolo, Macr. Rap. Com. 26 (2005) 1800-1804.

[43] R.K. Singal, M. Singal, R. Singal, Engineering Mechanics, I.K. International Publishing House Pvt. Ltd., New Delhi (2009).

[44] Y.C. Hsu, C.C. Wu, C.C. Lee, G.Z. Cao, I.Y. Shen, Sen. Actuat. A: Phys. 116 (2004) 369-377.

[45] B.V. Sankar, Compos. Sci. Technol. 61 (2001) 689-696.

[46] F.S. Foster, E.A. Harasiewicz, M.D. Sherar, IEEE T. Ultrason. Ferr. Freq. Con. 47 (2000) 1363-1371.

[47] F. Charette, A. Berry, C. Guigou, J. Acoust. Soc. Am. 103 (1998) 1493-1503.

[48] C. Domenici, D. Derossi, A. Bacci, S. Bennati, IEEE T. Electr. Insul. 24 (1989) 1077-1081.

[49] H.D. Espinosa, B.C. Prorok, J. Mat. Sci. 38 (2003) 4125-4128.

[50] S.U. Jen, T.C. Wu, Thin Solid Films 492 (2005) 166-172.

[51] A.C. Fischer-Cripps, Nanoindentation, Springer, New York (2004).

[52] K. Wang, S. Kundu, H. Lee, H. Liang, J. Phys. Chem., C 113 (2009) 8112-8117.

[53] G. Dehm, E. Arzt, Appl. Phys. Lett. 77 (2000) 1126-1128.

[54] K. Yamamoto, Y. Koga, S. Fujiwara, Diam. Relat. Mat. 10 (2001) 1921-1926.

[55] S. Kundu, Y.M. Wang, W. Xia, M. Muhler, J. Phys. Chem., C 112 (2008) 16869-16878.

[56] J.C.S. Wu, C.H. Chen, J. Photoch. Photobio., A 163 (2004) 509-515.

[57] M. Pakula, S. Biniak, A. Swiatkowski, Langmuir 14 (1998) 3082-3089.

[58] A.P. Terzyk, Coll. Surf., A 177 (2001) 23-45.

[59] M. Pakula, S. Biniak, A. Swiatkowski, S. Neffe, Carbon 40 (2002) 1873-1881.

[60] J. Grigas, E. Talik, M. Adamiec, V. Lazauskas, V. Nelkinas, J. Electron Spectrosc. 153 (2006) 22-29.

[61] Z. Yue, K.R. Benak, J.W. Wang, C.L. Mangun, J. Economy, J. Mat. Chem. 15 (2005) 3142-3148.

[62] S.F. Lim, Y.M. Zheng, J.P. Chen, Langmuir 25 (2009) 4973-4978.

[63] A. Derylo-Marczewska, A. Swiatkowski, B. Buczek, S. Biniak, Fuel 85 (2006) 410-417.

[64] J. Grigas, E. Tolik, Phys. Status Solidi, B 237 (2003) 494-499.

[65] E. Huger, K. Osuch, Europhys. Lett. 71 (2005) 276-282.

[66] S. Fuchs, T. Hahn, H.G. Lintz, Chem. Eng. Process 33 (1994) 363-369.

[67] D. Zemlyanov, B. Aszalos-Kiss, E. Kleimenov, D. Teschner, S. Zafeiratos, M. Havecker, A. Knop-Gericke, R. Schlogl, H. Gabasch, W. Unterberger, K. Hayek, B. Koltzer, Surf. Sci. 600 (2006) 983-994.

[68] H. Gabasch, W. Unterberger, K. Hayek, B. Klotzer, E. Kleimenov, D. Teschner, S. Zafeiratos, M. Havecker, A. Knop-Gericke, R. Schlogl, J.Y. Han, F.H. Ribeiro, B. Aszalos-Kiss, T. Curtin, D. Zemlyanov, Surf. Sci. 600 (2006) 2980-2989.

[69] J.F. Moulder, J. Chastain, Handbook of X-ray Photoelectron Spectroscopy: A Reference Book of Standard Spectra for Identification and Interpretation of XPS data, Physical Electronics, Eden Prairie, MN (1995).

[70] Materials Characterization Facility, Texas A&M University, Step-by-Step Instructions for XPS, <http://mcf.tamu.edu/docs/XPS_instructions.pdf>, (2009).

APPENDIX

X-ray photoelectron spectroscopy was employed to measure electron binding energy. A Kratos Axis Ultra Imaging instrument was utilized at the Materials Characterization Facility at Texas A&M University in College Station, TX. Figure 47 displays an image of the instrument.

Figure 47. The Kratos Ultra Axis Imaging instrument at the Materials Characterization Facility at Texas A&M University in College Station, TX.

The Kratos instrument is an extremely delicate machine; care must be taken in order to properly safely operate the device in order to prevent harm to the user as well as contamination. See Figure 17 for a schematic of the XPS process. It is necessary to continually check the pressures of three areas of the instrument. The first step is to properly load the sample into the instrument. Before the commencement of any measurements, the SAC must be in the range of 10^{-8} to 10^{-9} torr. Next, the STC must be in the range of 10^{-6} to 10^{-8} torr. Finally, the roughing pump must exist in the range from 10^{-2} to 10^{-3} torr. It is obligatory to clean the sample holder with acetone in order to remove all debris. It is important that no foreign objects other than the samples enter the chamber because any type of debris can contaminate the instrument. Next, the sample is mounted on the sample holder using double-sided conductive carbon tape. The user must ensure that the light at the end of the transfer rod is green as opposed to red. If the light at the end of the rod is red, then there is a risk that there will be an internal collision that can damage the claw that holds the sample holder. Figure 48 displays the transfer rod that is used to transfer the sample from the STC to the SAC, and the previously mentioned light is displayed in Figure 49.

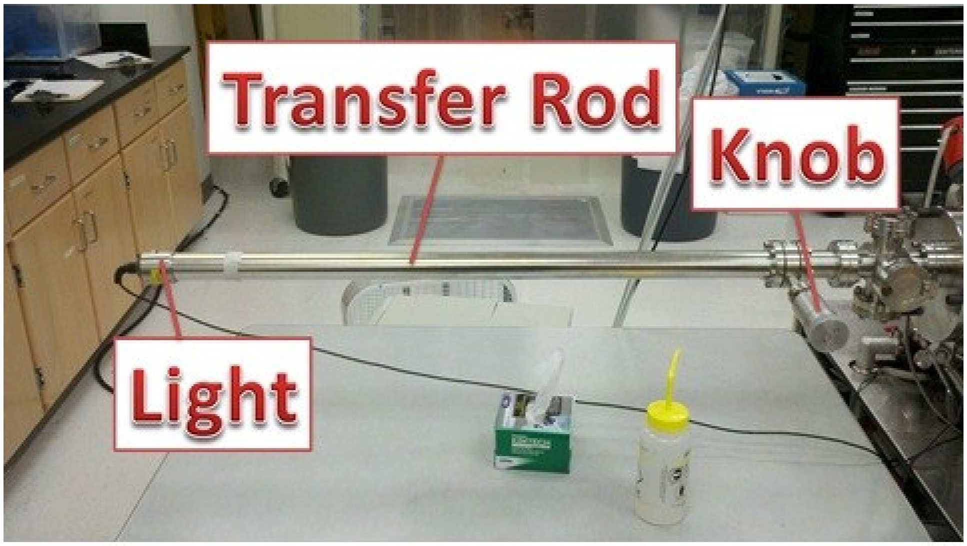

Figure 48. The figure displays the transfer rod that is used to transfer the sample from the STC to the SAC.

Figure 49. The figure displays the light at the end of the transfer rod.

Furthermore, in anticipation of placing the sample inside the STC chamber, the nitrogen tank must be opened in order to ensure suitable venting. There are screws on one end of the STC chamber door. The screws at the end of the chamber door must also be unscrewed in order to prevent massive damage to the system's framework. Two of the three screws are displayed in Figure 50.

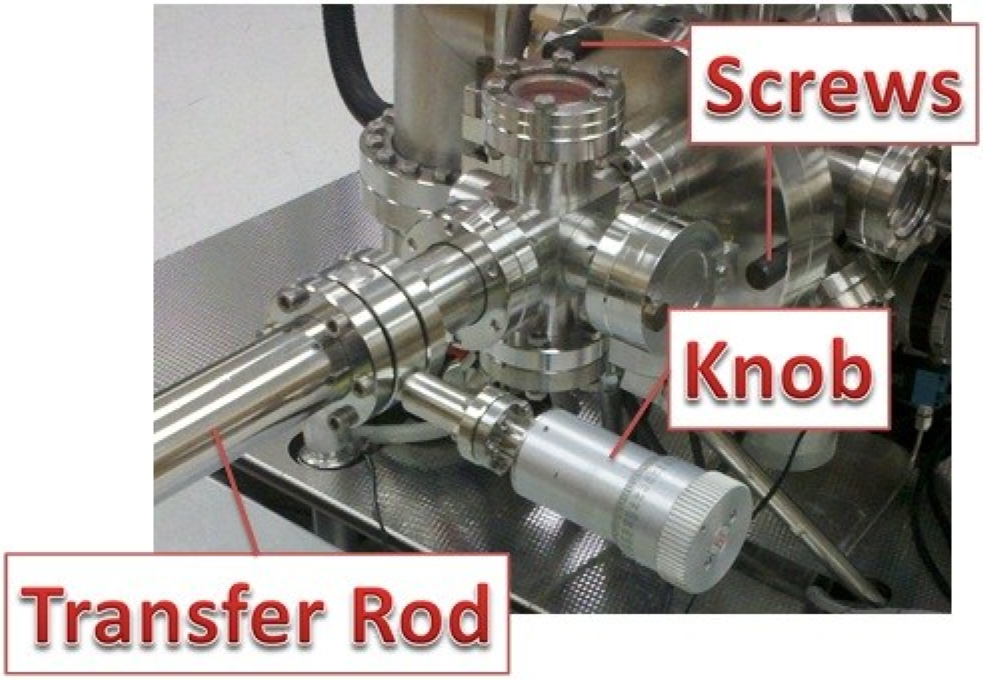

Figure 50. The aforementioned screws are displayed in the figure.

Subsequently, the operator must turn to the computer in order to make the necessary adjustments to increase the pressure inside of the STC chamber. The computer system is displayed in Figure 51.

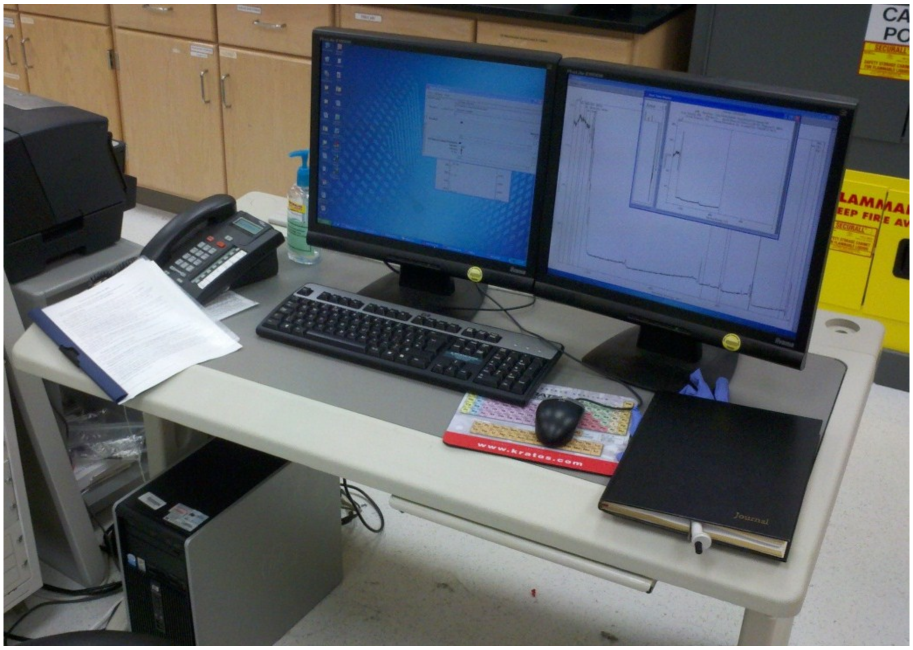

Figure 51. The computer system is displayed in the figure.

The user selects "Vent STC" in the "Vacuum Control" section of the "Instrument Manual Control" window. If the user remembered to unscrew the screws associated with the STC chamber, then the door should open after about a minute. The operator then turns the knob clockwise at the end of the STC chamber in order to reveal the claw. The light at the end of the transfer rod is now red. The sample is then loaded onto the claw and the user turns the knob counterclockwise to return the claw with the newly installed sample into the transfer rod. The user must ensure that the light is now green; otherwise, the claw will stick too far out of the transfer rod and cause problems in operation. The reader is referred to the Kratos Axis Ultra Imaging reference manual for all the details [41].

Next, the door to the STC must be closed and the screws tightened to ensure proper sealing. The operator must press “Pump STC” in the “Vacuum Control” section of the “Manual Control” window of the software in order to restore pressure to the STC chamber. Soon after “Pump STC” is pressed, the pressure gauge for the rough pump must reach 10^{-2} torr. Finally, before the sample is transferred from the STC to the SAC, the user must wait about fifteen minutes to three hours until the STC pressure reaches 9×10^{-7} torr [70].

After the sample has been loaded properly, it is obligatory to transfer the sample from the STC chamber into the SAC chamber in order to analyze the sample. It is necessary to ensure that the SAC chamber pressure is in the range of 10^{-8} to 10^{-9} torr and that the STC pressure is less than 9×10^{-7} torr. Next, the valve between the STC and SAC chambers is opened in order to provide an avenue to transfer the sample from the STC chamber to the SAC chamber. The operator subsequently turns the dial at the end of the transfer arm clockwise in order to transfer the sample from the SAC chamber to the STC chamber. It is then necessary to align the sample on the manipulator fork in the SAC chamber. This is accomplished through controlling the manipulator fork with a remote control. Once the sample is secured to the manipulator fork, the transfer arm is withdrawn from the SAC chamber by turning the knob at the end of the transfer arm cage counterclockwise. The operator knows that the transfer arm has been completely withdrawn to the necessary position when the light on the end of the transfer arm has turned from red to green. Next, it is necessary to close the valve between the STC chamber and the SAC chamber in order to prevent a dramatic increase in pressure in the

SAC chamber. In order for the location of incident X-rays to be coincident with the particular area of interest on the sample surface, the operator must move the manipulator stage using the remote control so that the area of interest is coincident with the “x” on the monitor [70].

After the sample has been successfully transferred from the STC into the SAC, there is a considerable amount of computer work necessary in order to properly analyze the sample. First, a new run is developed by clicking “New run” in the “Vision Instrument Manager” window. Subsequently, it is necessary to ensure that the file is saved in the operator’s directory. Each user maintains his own directory. This directory may be found by clicking “Browse”. After the directory is found, the user types the file name and clicks “Enter”. Next, the operator must name the page. This is accomplished by typing a name in the field at the top of the screen and pressing “Enter”. After the page is named, the user must paste the page into the flowchart by pressing the middle scroll button on the mouse while hovering in the flowchart area to the left. If this operation is performed properly, then there should exist a black rectangle with the corresponding page name in the flowchart to the left. It is then important to ensure that all of the parameters in the associated “Acquisition” section are properly entered. The following instructions apply for high resolution scans, which allow the user to observe individual peaks as opposed to the entire spectrum of peaks. The “Analyzer Mode” and “Lens Mode” should be set to “Spectrum” and “Hybrid”, respectively. The “Resolution” should be set to a pass energy of 20 and the “Aperture” should be set to “Slot”. The “Anode” employed is the “Mono (Al)”. The current is set to 10 mA and the “Anode HT (kV)” parameter is set to 12. The charge neutralizer is set to “on for acquisition” in order to correct for any charge imbalance. The “Type” field is set to “spectrum” with “Mono (Al)” selected for “B.E. Ref”. Finally, the “Energy regions” parameter is set to “on”. After completing the “Scan control” section to select the desired elements for XPS analysis, the user clicks the submit button to commence the process [70].

Once the data acquisition is complete, it is necessary to remove the sample. The user must open the valve between the STC and SAC. The operator then uses the remote control to transfer the sample holder from the manipulator to the claw. Subsequently, the user withdraws the claw from the SAC. The screws displayed in Figure 50 must again be unscrewed and the valve between the STC and SAC must be closed. The STC is then vented in order to increase the pressure, and the chamber door opens. The sample is removed by turning the knob clockwise to reveal the claw. Next, the claw is returned to its original position by turning the knob counterclockwise, and the chamber door is closed. The screws are tightened in place, and the STC is pumped to decrease the pressure. Finally, the X-ray gun is switched off [70].

VITA

Nicholas Joseph Nudo received his Bachelor of Science degree in mechanical engineering from Texas A&M University in 2009. He received the 2009 Caddess Award as the top graduate in the area of materials sciences in the department of mechanical engineering at Texas A&M University in the Class of 2009. He received a Master of Science degree in mechanical engineering from Texas A&M University in 2011. His research interests include the broad area of materials science and engineering and X-ray photoelectron spectroscopy in particular. He will begin work in the summer of 2011 as Engineer II at Baker Hughes in Houston, TX. Mr. Nudo may be reached at the Department of Mechanical Engineering, c/o Dr. Hong Liang, Texas A&M University, College Station, TX, 77845-3123.